

Journal Pre-proofs

Multiscale modelling of diffusion and enzymatic reaction in porous electrodes in Direct Electron Transfer mode

T.D. Le, D. Lasseux, L. Zhang, C. Carucci, S. Gounel, S. Bichon, F. Lorenzutti, A. Kuhn, T. Šafarik, N. Mano

PII: S0009-2509(21)00722-3
DOI: <https://doi.org/10.1016/j.ces.2021.117157>
Reference: CES 117157

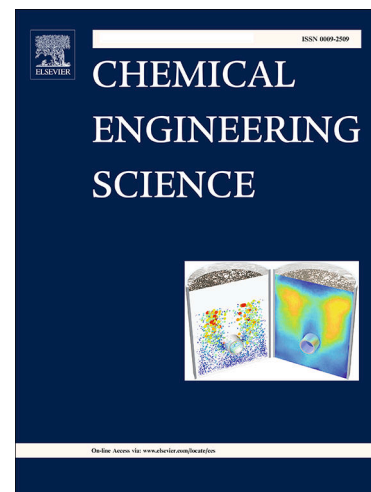
To appear in: *Chemical Engineering Science*

Received Date: 6 June 2021
Accepted Date: 27 September 2021

Please cite this article as: T.D. Le, D. Lasseux, L. Zhang, C. Carucci, S. Gounel, S. Bichon, F. Lorenzutti, A. Kuhn, T. Šafarik, N. Mano, Multiscale modelling of diffusion and enzymatic reaction in porous electrodes in Direct Electron Transfer mode, *Chemical Engineering Science* (2021), doi: <https://doi.org/10.1016/j.ces.2021.117157>

This is a PDF file of an article that has undergone enhancements after acceptance, such as the addition of a cover page and metadata, and formatting for readability, but it is not yet the definitive version of record. This version will undergo additional copyediting, typesetting and review before it is published in its final form, but we are providing this version to give early visibility of the article. Please note that, during the production process, errors may be discovered which could affect the content, and all legal disclaimers that apply to the journal pertain.

© 2021 Published by Elsevier Ltd.



Highlights

- A macroscopic model for enzymatic porous electrode operating in DET mode is derived
- The upscaled model is validated with pore-scale direct numerical simulations
- Macroscopic model predictions are validated by comparisons with experimental data

Journal Pre-proofs

Multiscale modelling of diffusion and enzymatic reaction in porous electrodes in Direct Electron Transfer mode

T. D. Le

I2M, UMR 5295, CNRS, Univ. Bordeaux, 351, Cours de la Libération, 33405 Talence CEDEX, France

University of Lorraine, CNRS, LEMTA, F-54000 Nancy, France

D. Lasseux*

I2M, UMR 5295, CNRS, Univ. Bordeaux, 351, Cours de la Libération, 33405 Talence CEDEX, France

L. Zhang

Univ. Bordeaux, CNRS, Bordeaux INP, ISM UMR 5255, Site ENSCBP, 16 Avenue Pey Berland, 33607 Pessac, France

C. Carucci

Univ. Bordeaux, CNRS, Bordeaux INP, ISM UMR 5255, Site ENSCBP, 16 Avenue Pey Berland, 33607 Pessac, France

S. Gounel

Centre de Recherche Paul Pascal, CNRS UMR5031, University of Bordeaux, Avenue Albert Schweitzer, 33600 Pessac, France

S. Bichon

Centre de Recherche Paul Pascal, CNRS UMR5031, University of Bordeaux, Avenue Albert Schweitzer, 33600 Pessac, France

F. Lorenzutti

I2M, UMR 5295, CNRS, Univ. Bordeaux, 351, Cours de la Libération, 33405 Talence CEDEX, France

A. Kuhn

Univ. Bordeaux, CNRS, Bordeaux INP, ISM UMR 5255, Site ENSCBP, 16 Avenue Pey Berland, 33607 Pessac, France

T. Šafarik

*Corresponding author

Email addresses: tien-dung.le@univ-lorraine.fr (T. D. Le), didier.lasseux@u-bordeaux.fr (D. Lasseux), lin.zhang@henu.edu.cn (L. Zhang), cristina.carucci@unica.it (C. Carucci), sebastien.gounel@crpp.cnrs.fr (S. Gounel), sabrina.bichon@crpp.cnrs.fr (S. Bichon), francesca.lorenzutti@epfl.ch (F. Lorenzutti), kuhn@enscbp.fr (A. Kuhn), tatjana.safarik@u-bordeaux.fr (T. Šafarik), nicolas.mano@crpp.cnrs.fr (N. Mano)

*Univ. Bordeaux, CNRS, Bordeaux INP, ISM UMR 5255, Site ENSCBP, 16 Avenue Pey Berland, 33607
Pessac, France*

N. Mano

*Centre de Recherche Paul Pascal, CNRS UMR5031, University of Bordeaux, Avenue Albert Schweitzer,
33600 Pessac, France*

Abstract

This work is dedicated to a multi-scale modelling of coupled diffusion and reaction in a porous micro-electrode operating in the Direct Electron Transfer mode. The pore-scale physico-electrochemical unsteady model is developed considering the oxygen reduction, catalyzed by an enzyme coating the pores of the electrode, coupled to the diffusion of oxygen and mass balance of enzymes. This model is formally upscaled to obtain an original closed unsteady macroscopic model operating at the electrode scale, together with the associated closure providing the effective diffusivity tensor. A validation of this model is carried out from a comparison with the solution of the initial 3D pore-scale governing equations considering the bilirubin oxydase as the catalyst. The relevance and accuracy of the macroscale model are proved allowing a considerable simulation speedup. It is further employed to successfully predict experimental voltammetry results obtained with porous gold electrodes functionalized with a bilirubin oxidase mutant (BOD S362C). This model represents a breakthrough by providing an operational simple way of understanding and further optimizing porous electrodes functioning in DET mode.

Key words: Porous electrode, Direct Electron Transfer, Bilirubin Oxidase, Diffusion reaction, Volume averaging method

1. Introduction

Over the past two decades, porous electrodes, featuring a high specific surface area (*i.e.* a large internal solid-fluid interface per unit volume), have been efficiently developed to make miniaturized electro-devices such as bio-batteries, bio-actuators and bio-sensors [1–4]. Such electrodes can provide electrical current several orders of magnitude larger than simple flat electrodes of the same size [5, 6]. A classical way to synthesize porous electrodes is to form an ordered assembly of beads, for example by employing the Langmuir-Blodgett technique [7] and use it as a template as proposed by Bartlett et al. [8]. Electrodeposition of a conducting material is then performed through the layered bead assembly, followed by beads dissolution, yielding an inverse opale structure constitutive of the electrode [9]. Due to its versatility, this technique may be employed to obtain porous microstructures with tunable porosity and controllable architecture [2].

For applications in biofuel cells [10–17], redox reactions can be catalyzed by enzymes which, in order to enhance their lifetime and stability, may be immobilized by entrapping

15 the proteins [18, 19]. This can be achieved using different techniques, like entrapment in
16 a conducting polymer matrix occupying a more or less significant fraction of the pores, or
17 adsorption at the pore surfaces [20–22], eventually combined with nano-structuration of the
18 surfaces [23, 24]. In the former case, a mediator is employed to shuttle the electrons to and
19 from the electrode’s internal surfaces, giving rise to a so-called Mediated Electron Transfer
20 (MET) process. In contrast, in the latter case, when enzymes are adsorbed on the reactive
21 surfaces so that their active centers are positioned within the electron tunnelling distance
22 of the current collector surfaces, the process is referred to as a Direct Electron Transfer
23 (DET). In that case, no mediator is involved. A typical configuration for such a biofuel
24 cell is such that the two electrodes are modified by bioelectrocatalysts. For example at the
25 cathode, the multicopper oxidases (MCOs) such as bilirubin oxidase (BOD) are adsorbed
26 on the electrode surface. They consist of a type 1 copper (T1) site which directly accepts
27 electrons from the electrode, and type 2 and type 3 copper, so-called trinuclear center (TNC
28 site), receiving electrons from T1. The oxygen is then reduced to water at TNC sites [15, 25].
29 The process will be further detailed in section 2.1. In this example, chemical energy is drawn
30 from the oxygen-glucose couple, which naturally exists in physiological fluids for instance,
31 and is converted into electrical energy resulting from oxygen reduction at the cathode and
32 glucose oxidation at the anode.

33 Modelling of transport and reactions in porous electrodes has often been treated with
34 empirical macroscopic models even in the case without enzymes (see for instance [26–30]).
35 As a consequence, all the features of the physico-electrochemical mechanisms (coupling dif-
36 fusion and reaction in the unsteady regime for example) and of the geometrical structure, in
37 particular for porous electrodes, are not elucidated. More formal approaches were proposed
38 [31–33] without however any explicit closure to relate the pore-scale microstructure to the
39 effective macroscale parameters, in particular, the effective diffusivity. In a recent work, a
40 thorough multiscale model for direct oxygen reduction reaction in a porous electrode was
41 developed by upscaling the pore-scale model and formally obtain a closed macroscale de-
42 scription using the volume averaging method [34]. It was employed to determine the optimal
43 macroscopic thickness of a porous electrode [35, 36] and it has been extended to the case of
44 two serial reactions for oxygen reduction [37].

45 In the case of reactions catalyzed by enzymes in the DET (or MET) mode, modelling is
46 more complex, and this has motivated empirical analytic expressions of the current density
47 to fit experimental data curves [38, 39]. Moreover, in these works, steady-state conditions
48 were assumed for which surface concentrations of enzymes are supposed to be constant and
49 oxygen supply is continuous. Some other studies were carried for a simple shape non-porous
50 electrode, assuming steady-state [40] or non steady-state conditions [41]. In an interesting
51 work by Do *et al.* [42], a non-steady macroscopic model was proposed. The reported model
52 is 1D and electrode scale equations are not explicitly derived, remaining unclosed since the
53 effective diffusion coefficient is empirically correlated to the porosity of the material. The
54 model was successfully tested to predict experimental observations in steady-state conditions.
55 For practical use, a general 3D unsteady and closed macroscopic model operating at the
56 electrode scale is highly desirable, including all the available information of the physico-

57 electrochemical processes at the underlying pore-scale.

58 In this context, the present work aims at a detailed multiscale modelling of a porous
 59 electrode operating in the DET mode, following an upscaling approach. The development
 60 represents a complex task due to the coupling of reactions, unsteadiness and non linearity
 61 of the overall problem. The purpose is first to provide the set of balance equations, initial
 62 and boundary conditions governing the transient coupled process for oxygen diffusion and
 63 catalyzed enzymatic reactions in the DET regime within the pores. In this configuration, the
 64 pore-scale mass transfer of oxygen is essentially diffusive, while a cathodic oxygen reduction
 65 reaction with enzymatic catalysis is considered partially using the framework proposed by
 66 Hexter and co-workers [43, 44] for the reaction scheme. Upscaling is performed with the vol-
 67 ume averaging method [45] to obtain a new and original macroscopic model at the electrode
 68 scale that is further validated both numerically and with experimental data. This model is
 69 fully unsteady, yielding the evolution of both the enzyme and oxygen concentrations. It is
 70 formally derived from the pore-scale equations with a closure providing the effective param-
 71 eters. This approach has not been reported in the literature so far although this is of prime
 72 importance as was raised as a conclusion in a recent review by Rajendran *et al.* [46].

73 The remainder of the article is organized as follows. In Section 2, the pore-scale diffu-
 74 sion/reaction model at the microscale is developed for the enzymatic Direct Electron Transfer
 75 regime. In this context, an electrochemical model for the reduction reaction of oxygen cat-
 76 alyzed by BOD is proposed. It is coupled to mass transfer by diffusion of oxygen and mass
 77 balance of enzyme under non steady-state conditions. To derive a macroscopic model that
 78 is much more effective in terms of computational resources, an upscaling procedure of the
 79 pore-scale model is applied, the main steps of which are summarized in Section 3 for the
 80 sake of conciseness. More details for this derivation are reported in Appendix A. In Section
 81 4, 3D direct numerical simulations of the pore-scale model are carried out and their results
 82 are compared to those obtained from simulations of the 1D macroscopic model to validate
 83 the upscaling approach. Experimental details, describing the materials and methods for the
 84 electrocatalytic characterization of macroporous gold electrodes are provided in Section 5.
 85 The ability of the macroscopic model to predict experimental voltammetry results, obtained
 86 from these electrodes modified by BOD adsorption and immersed in a buffer solution, is
 87 presented in this section. Conclusions are proposed in Section 6.

88 2. Pore-scale diffusion/reaction coupled model

89 In this section, the unsteady pore-scale model for diffusion and reaction in a porous
 90 electrode, whose internal surface has been modified by the adsorption of BOD enzyme, is
 91 developed. The oxygen reduction reaction scheme within the layer containing the enzyme
 92 at the electrode surface is assumed to take place in the DET mode. Without any restriction
 93 in the physical description of the electrochemical process, the analysis is carried out at the
 94 cathode.

95 The porous electrode, immersed in a reactive solution, occupies the spatial domain Ω
 96 composed of the solid phase Ω_s and the fluid phase Ω_f with the interface denoted by $\Gamma_{sf} =$
 97 $\Omega_f \cap \Omega_s$ nearby which the oxygen reduction reaction takes place. The electrode is supplied by

98 diffusion of oxygen from the bulk fluid, occupying the domain Ω_e , surrounding the electrode.
 99 Electron exchange during the reduction of oxygen results from a double electron transfer
 100 which may be described by a pair of reactions as proposed in section 2.1.

101 2.1. Electrochemical process

102 The BOD enzyme is supposed to be immobilized at the surface Γ_{sf} of the cathodic
 103 electrode to catalyze the oxygen reduction. It contains type 1 copper, forming T1 sites,
 104 while TNC sites are composed of type 2 and type 3 copper [14]. In the DET mode, electrons
 105 from the electrode's internal surface are accepted by type 1 copper (T1 sites) where the
 106 enzyme reduction occurs. They are transferred from T1 to the TNC (T2 and T3) sites
 107 which remain at a tunneling distance from the pore surfaces and where reduction of oxygen
 108 takes place [25, 38] (see Fig. 1). The reaction scheme at an electrode surface modified with
 109 BOD may hence be described following the approach proposed by Hexter and co-workers
 110 [43, 44] for the reaction of hydrogenases during the reduction of H^+ to H_2 . In these works,
 111 the electrode is supposed to be continuously supplied with H^+ so that the mass transfer
 112 problem is neglected yielding a description under steady-state conditions. On the contrary,
 113 a fully unsteady description is considered here.

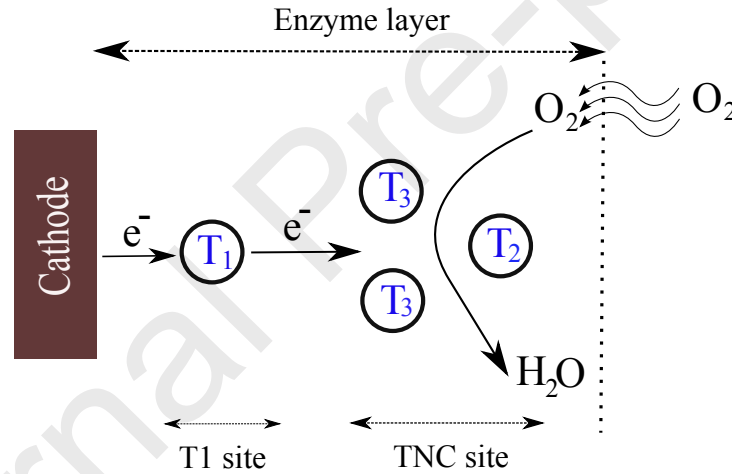
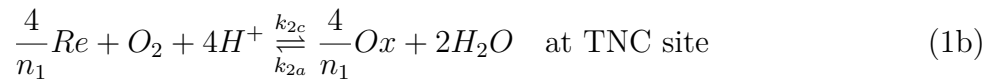


Figure 1: Schematic representation of electron transfer from the electrode surface to the T1 site and further to a TNC site where oxygen reduction occurs

114 In the case of oxygen reduction of interest here, the catalytic reaction in the DET mode
 115 may be written in the following form



where n_1 is the number of transferred electrons involved in the reduction of the enzyme which oxidized and reduced forms are denoted by Ox and Re respectively. In the case of

BOD, which is further considered for validation and comparison with experiments in sections 4 and 5, $n_1 = 1$ [38]. Note that the direct reaction pathway for oxygen reduction has been assumed in (1b) as this was confirmed to be the preferential one in experimental observations with the BOD enzyme [47]. The electron transfer rate constants k_{1a} and k_{1c} are given by the Butler-Volmer relationships

$$k_{1c} = k_0 \exp \left[-\frac{n_1 \alpha_1 F (E - E_{Ox/Re}^0)}{RT} \right] \quad (2a)$$

$$k_{1a} = k_0 \exp \left[\frac{n_1 (1 - \alpha_1) F (E - E_{Ox/Re}^0)}{RT} \right] \quad (2b)$$

where k_0 and α_1 are the standard rate constant and electron transfer coefficient, E and $E_{Ox/Re}^0$ the electrode potential and the potential of the redox center, F , R and T the Faraday's constant, gas constant and temperature respectively. Similarly, for the oxygen reduction, the catalytic rate constants k_{2c} and k_{2a} , representative of the internal driving energy within the enzyme, take the following expressions

$$k_{2c} = k'_2 \exp \left[\frac{-n_2 \alpha_2 F (E_{Ox/Re}^0 - E_{O_2/H_2O})}{RT} \right] \quad (3a)$$

$$k_{2a} = k_2 \exp \left[\frac{n_2 (1 - \alpha_2) F (E_{Ox/Re}^0 - E_{O_2/H_2O})}{RT} \right] \quad (3b)$$

116 where E_{O_2/H_2O} is the thermodynamic equilibrium potential of the couple O_2/H_2O , α_2 the
 117 electron transfer coefficient associated with this reaction and n_2 the number of electrons
 118 involved. It should be noted that the oxygen reduction in reaction (1b) can be considered
 119 as irreversible. For both the validation of the macroscopic model and the comparison with
 120 experiments presented in the following sections, the backward reaction in (1b) is ignored and
 121 k_{2a} was hence taken equal to zero for consistency, even if this parameter is formally kept for
 122 completeness in the theoretical development reported below, which may straightforwardly
 123 be used for an other type of system.

Although four electrons are required for the reduction of O_2 in (1b), a different value might be relevant for n_2 depending on the limiting step governing the electron transfer for this reaction. A further detailed discussion of this feature is beyond the scope of the present work and, as will be seen later, the use of the models derived in the following sections does not explicitly require the value of n_2 to be specified. In addition, it is worth noticing that the unit of the rate constants k_{1c} , k_{1a} and k_{2a} is $1/s$ whereas that of k_{2c} is $m^3/mol/s$. The latter is in contrast with that of the corresponding constant used in the work by Hexter *et al.* [43] which was restricted to steady conditions that are not retained here as this might be insufficient in practical situations. From the oxygen reduction reaction at TNC sites (see (1b)), the associated reaction rate, R_{O_2} , can be expressed according to the following Butler-Volmer relationship [48]

$$R_{O_2} = -k_{2c} c_{Re} c_{O_2} + k_{2a} c_{Ox} \quad (4)$$

124 In the following, a fully coupled diffusion-reaction model is developed, in which concentra-
 125 tions of all species (enzyme and oxygen) are time-dependent to describe the entire unsteady
 126 process.

127 2.2. Physical model at the pore-scale

128 Modelling starts with the initial and boundary value problem governing diffusion of
 129 oxygen, which is assumed to be a Fickian process, coupled to oxido-reduction mechanisms
 130 inside the pores. Since the enzyme is immobilized at the pore surfaces, no diffusion is taken
 131 into account for this species. The pore-scale model can hence be written as follows

$$\frac{\partial c_{Re}}{\partial t} = k_{1c}c_{Ox} - k_{1a}c_{Re} - k_{2c}c_{Re}c_{O_2} + k_{2a}c_{Ox} \quad \text{at } \Gamma_{sf} \quad (5a)$$

$$c_{Ox} + c_{Re} = c_E^t \quad \text{at } \Gamma_{sf} \quad (5b)$$

$$\text{I.C.1} \quad c_{Re} = \mathcal{F}_{Re}(\mathbf{r}) \quad \mathbf{r} \in \Gamma_{sf}, t = 0 \quad (5c)$$

$$\frac{\partial c_{O_2}}{\partial t} = \nabla \cdot (\mathcal{D}_{O_2} \nabla c_{O_2}) \quad \text{in } \Omega_f \quad (5d)$$

$$\text{B.C.1} \quad -\mathbf{n} \cdot \mathcal{D}_{O_2} \nabla c_{O_2} = -R_{O_2} \quad \text{at } \Gamma_{sf} \quad (5e)$$

$$\text{I.C.2} \quad c_{O_2} = \mathcal{F}_{O_2}(\mathbf{r}) \quad \mathbf{r} \in \Omega_f, t = 0 \quad (5f)$$

$$\text{B.C.2} \quad c_{O_2} = \mathcal{G}_{O_2}(\mathbf{r}, t) \quad \mathbf{r} \in A_{fe}, \forall t \quad (5g)$$

where c_{Re} , c_{Ox} and c_{O_2} are the surface concentrations of Re and Ox and the bulk oxygen concentration respectively. The total enzyme concentration c_E^t (see Eq. (5b)) is considered to remain constant at any time whereas mass conservation of Re in Eq. (5a) results from reactions (1). In the oxygen mass conservation equation (5d) and in the boundary condition in Eq. (5e), \mathcal{D}_{O_2} is the molecular diffusion coefficient of O_2 in the fluid saturating the pores while \mathbf{n} is the unit normal vector to Γ_{sf} pointing out of Ω_f . The reaction rate, R_{O_2} , is given by Eq. (4). In the expression of the external boundary condition B.C.2, $A_{fe} = \Omega_f \cap \Omega_e$ is the entrance and/or exit boundaries of the fluid phase, Ω_f , from/into the external bulk fluid, Ω_e , in which the electrode is immersed. The solution of Eqs. (5) yields the oxygen and enzymes concentration fields from which the current density, j , can be obtained from the reaction rate at T1 sites (1a). It is given by

$$j = n_1 F (k_{1a}c_{Re} - k_{1c}c_{Ox}) \quad (6)$$

that can be further used to compute the total current, I , available at the electrode according to

$$I = \int_{\Gamma_{sf}} j dS \quad (7)$$

132 Although the solution of Eqs. (5) can be sought using a Direct Numerical Simulation (DNS)
 133 as will be reported for validation purposes in section 4.1, a macroscopic model is necessary
 134 for the characterization and prediction of the behavior of an electrode. Moreover, as in-
 135 dicated in a previous work dedicated to modelling of electrodes in the absence of enzyme
 136 [34], computational resources required by DNS are substantial and a macroscopic model is

137 much more efficient for practical use. With these objectives in mind, the pore-scale model is
 138 upscaled, carrying coupling and non linearities, in order to obtain a macroscopic description
 139 that is provided in the next section.

140 3. Macroscopic model

141 The macroscopic model, operating at the electrode scale, is derived from the initial and
 142 boundary value pore-scale problem using the volume averaging method [45]. For the sake
 143 of brevity, only the main result of this procedure is reported below while the details of the
 144 formal derivation are provided in Appendix A.

Let V , of measure V and size r_0 , be the averaging volume including the solid and fluid domains V_s and V_f (of volumes V_s and V_f , respectively) sharing the solid/fluid interface A_{sf} of measure A_{sf} . The porosity, ε_f , and specific area, a_v , of the porous material are respectively defined by

$$\varepsilon_f = V_f/V \quad (8a)$$

$$a_v = A_{sf}/V \quad (8b)$$

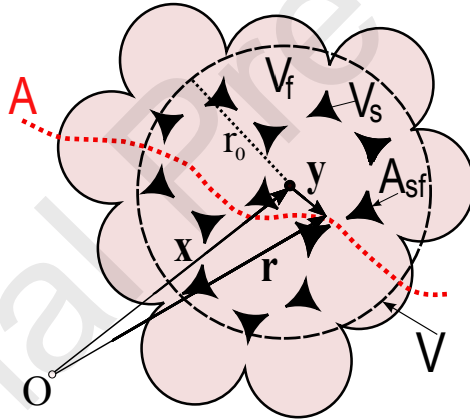


Figure 2: Averaging volume for a two-phase system.

The upscaling process makes use of the superficial, intrinsic and area averages of the concentration fields for oxygen and reduced enzyme that are respectively defined by

$$\langle c_{O_2} \rangle |_{\mathbf{x}} = \frac{1}{V} \int_{V_f(\mathbf{x})} c_{O_2} |_{\mathbf{x}+\mathbf{y}} dV \quad (9a)$$

$$\langle c_{O_2} \rangle^f |_{\mathbf{x}} = \frac{1}{V_f} \int_{V_f(\mathbf{x})} c_{O_2} |_{\mathbf{x}+\mathbf{y}} dV \quad (9b)$$

$$\langle c_X \rangle_{sf} |_{\mathbf{x}} = \frac{1}{A_{sf}} \int_{A_{sf}(\mathbf{x})} c_X |_{\mathbf{x}+\mathbf{y}} dA, \quad X = O_2, Re \quad (9c)$$

with the straightforward relationship $\langle c_{O_2} \rangle = \varepsilon_f \langle c_{O_2} \rangle^f$ and where \mathbf{x} locates the centroid of the averaging volume while $\mathbf{y} = \mathbf{r} - \mathbf{x}$ locates any point within V_f relative to \mathbf{x} (see Fig. 2). For the sake of simplicity, the subscript referring to the location may be dropped, unless necessary. The derivation of the upscaled model is subject to a scale hierarchy defined by $\ell_p \ll r_0 \ll L$, ℓ_p being the characteristic pore size and L the macroscopic size of the electrode. The upscaling procedure is carried out according to the four main steps reported in Appendix A and under the constraints on the kinetic number, Ki , and time scale respectively given by

$$Ki = \frac{k_{2c} \ell_p c_E^t}{\mathcal{D}_{O_2}} \ll 1 \quad (10a)$$

$$t \gg \mathcal{O} \left[\frac{\ell_p^2}{\mathcal{D}_{O_2}}, \frac{1}{k_{1c} + k_{1a} + k_{2a} + k_{2c} \langle c_{O_2} \rangle^f} \right] \quad (10b)$$

145

Under these circumstances, the macroscopic model, including the enzyme and oxygen effective mass conservation equations operating at the electrode scale, can be written as

$$\frac{\partial \langle c_{Re} \rangle_{sf}}{\partial t} = - (k_{1c} + k_{1a} + k_{2a}) \langle c_{Re} \rangle_{sf} - k_{2c} \langle c_{Re} \rangle_{sf} \langle c_{O_2} \rangle^f + (k_{1c} + k_{2a}) c_E^t \quad (11a)$$

$$\langle c_{Ox} \rangle_{sf} = c_E^t - \langle c_{Re} \rangle_{sf} \quad (11b)$$

$$\varepsilon_f \frac{\partial \langle c_{O_2} \rangle^f}{\partial t} = \nabla \cdot (\varepsilon_f \mathbf{D}_{eff} \cdot \nabla \langle c_{O_2} \rangle^f) - k_{2c} a_v \langle c_{O_2} \rangle^f \langle c_{Re} \rangle_{sf} - k_{2a} a_v (\langle c_{Re} \rangle_{sf} - c_E^t) \quad (11c)$$

146

147

148

149

150

151

152

153

154

155

156

157

The constraints expressed in (10) indicate that, strictly speaking, the averaged model can provide accurate predictions of the oxygen and enzyme average concentrations in the mass transfer limited regime (10a) and for times larger than the overall reaction kinetics characteristic time (10b). First, it must be noted that, despite the closure can be treated as a steady problem with these assumptions, the macroscale model remains unsteady, and this is because the time scales of variation of the average and pore-scale concentrations are different. Secondly, it must be emphasized that these constraints are usually overly severe and, most of the time, the range of applicability of the model can be extended beyond these constraints, *i.e.*, for $Ki \sim 1$ and $t \sim \mathcal{O} \left[\frac{\ell_p^2}{\mathcal{D}_{O_2}}, \frac{1}{k_{1c} + k_{1a} + k_{2a} + k_{2c} \langle c_{O_2} \rangle^f} \right]$ (see for instance [49, 50] for similar but somewhat different problems). Nevertheless, this deserves a careful analysis that is beyond the scope of this work.

In the macroscopic diffusion-reaction equation (11c), \mathbf{D}_{eff} is the effective diffusion tensor (that is symmetric [51]), given by

$$\mathbf{D}_{eff} = \mathcal{D}_{O_2} \left(\mathbf{I} + \frac{1}{V_f} \int_{A_{sf}} \mathbf{n} b dA \right) \quad (12)$$

in which \mathbf{I} is the identity tensor and \mathbf{nb} denotes the outer product between the two vectors \mathbf{n} and \mathbf{b} , \mathbf{b} , the latter being solution of the following closure problem (see also Eqs. (A.33) in Appendix A)

$$\nabla^2 \mathbf{b} = 0 \quad \text{in } \mathbf{V}_f \quad (13a)$$

$$\mathbf{n} \cdot \nabla \mathbf{b} = -\mathbf{n} \quad \text{at } \mathbf{A}_{sf} \quad (13b)$$

$$\langle \mathbf{b} \rangle^f = 0 \quad (13c)$$

$$\mathbf{b}(\mathbf{r}) = \mathbf{b}(\mathbf{r} + \ell_i \mathbf{e}_i) \quad i = 1, 2, 3 \quad (13d)$$

158 This problem is intrinsic to the porous structure, which means that its solution only depends
159 on the microgeometry of the pore space. To obtain this result, it must be noted that
160 the averaging domain, \mathbf{V} , was taken as a Representative Elementary Volume of the porous
161 structure that was further considered as pseudo periodic so that the closure problem is solved
162 on a unit cell whose periodic lattice vectors are $\ell_i \mathbf{e}_i$ ($i = 1, 2, 3$).

163 It should be noted that the closure performs the essential link between the micro- and
164 macroscale models. Indeed, the closure problem given in Eqs. (13) contains the nonredun-
165 dant information (in particular the microstructure implied in \mathbf{V}_f and \mathbf{A}_{sf}) that is essential
166 in the macroscopic model. As a result, Eqs. (11), together with the initial and bound-
167 ary conditions on $\langle c_{Re} \rangle_{sf}$ and $\langle c_{O_2} \rangle^f$, form the new macroscopic effective model of coupled
168 diffusion-reaction for a porous electrode operating in the DET mode.

The expression of the current from the macroscopic surface average of the reduced enzyme concentration can now be derived. The surface average of Eq. (6) yields

$$\langle j \rangle_{sf} = n_1 F \left(k_{1a} \langle c_{Re} \rangle_{sf} - k_{1c} \left(c_E^t - \langle c_{Re} \rangle_{sf} \right) \right) \quad (14)$$

from which the current per unit volume of the unit cell representative of the medium, i_v , can be deduced as $i_v = \langle j \rangle_{sf} A_{sf} / V = a_v \langle j \rangle_{sf}$. The total current, I , delivered by the electrode is hence given by $I = \int_{\Omega} i_v dV$, *i.e.*

$$I = a_v \int_{\Omega} \langle j \rangle_{sf} dV \quad (15)$$

169 4. Numerical results and discussions

170 The relevance of the prediction obtained with the new original macroscopic model is
171 assessed by a comparison with DNS of the pore-scale problem. This is carried out on a model
172 porous structure whose unit cell, of size ℓ_R , is a face-centered cubic (FCC) arrangement of
173 spherical pores, of diameter $d_s \equiv \ell_p$, interconnected to each other through circular windows
174 of diameter d_c (see Fig. 3). The objective of this procedure is to validate the macroscopic
175 model so that it can be used in place of the pore-scale model with an expected important
176 gain in performance.

177 4.1. Direct numerical simulation of the pore-scale model

178 The 3D numerical voltammetry experiments were performed on a computational domain
 179 represented in Fig. 3. The porous electrode is composed of periodic FCC unit cells in
 180 the z -direction, between $z = -L_e$, where the electrically conducting electrode support is
 181 positioned, and $z = 0$, where the electrode is in contact with the bulk fluid saturating the
 182 pores. The fluid region, Ω_e , between $z = 0$ and $z = L_N$, corresponds to the diffusion layer
 183 where oxygen molecular diffusion takes place. Periodic boundary conditions are applied in
 184 the x and y directions. This is justified by the fact that the electrode length is supposed to
 185 be much larger than ℓ_R and that the same holds for its lateral extension, if the electrode is
 186 a plane one. If it is circular, L_e is supposed to be much smaller than its mean radius. A
 187 zero flux condition is imposed at $z = -L_e$ while a constant oxygen concentration, $c_{O_2} = c_{O_2}^0$,
 188 is considered at the interface of the diffusion layer with the rest of the bulk fluid, $z = L_N$.
 189 The initial concentration of oxygen is supposed to be uniform equal to $c_{O_2}^0$. In addition, only
 190 oxidized enzyme is assumed to be present at the initial state, leading to $c_{Re} = 0$ at $t = 0$.

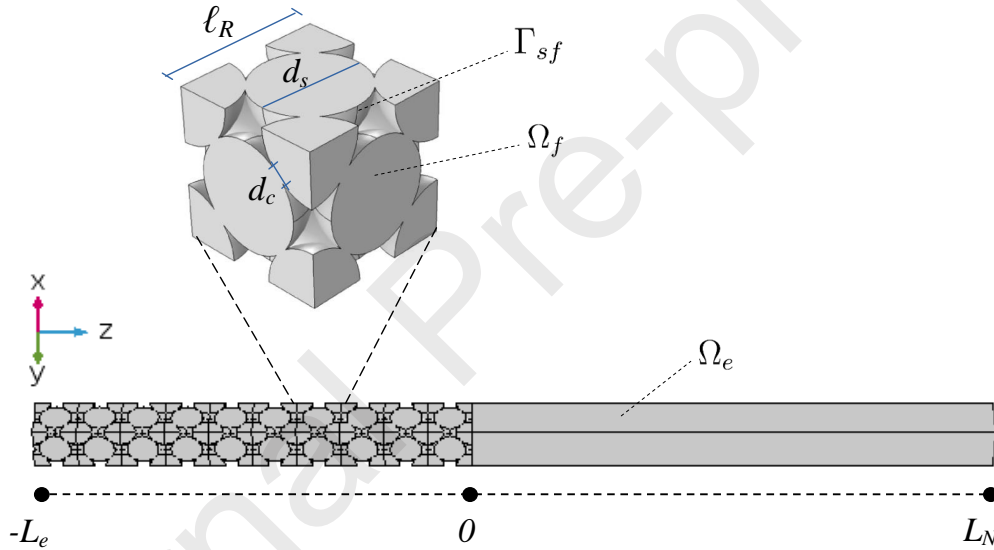


Figure 3: 3D domain for the direct numerical simulation.

The pore-scale problem in Eqs. (5), coupled to the diffusion of O_2 in the diffusion layer, can be rewritten in a dimensionless form using ℓ_R , $\frac{\ell_R^2}{D_{O_2}}$, $c_{O_2}^0$ and c_E^t as the reference length, time, oxygen and enzyme surface concentrations. Denoting dimensionless quantities with

the superscript $*$, this coupled non-linear problem is given by

$$\begin{aligned} \frac{\partial c_{O_2}^*}{\partial t^*} &= \nabla^{*2} c_{O_2}^* && \text{in } \Omega_f \cup \Omega_e && (16a) \\ \text{B.C.1} \quad -\mathbf{n} \cdot \nabla^* c_{O_2}^* &= 0 && \text{at } z^* = -L_e^* && (16b) \\ \text{B.C.2} \quad c_{O_2}^* &= 1 && \text{at } z^* = L_N^* && (16c) \\ \text{B.C.3} \quad -\mathbf{n} \cdot \nabla^* c_{O_2}^* &= \frac{\ell_{RC}^t}{D_{O_2}} \left(k_{2c} c_{Re}^* c_{O_2}^* - \frac{k_{2a}}{c_{O_2}^0} (1 - c_{Re}^*) \right) && \text{at } \Gamma_{sf} && (16d) \\ \frac{\partial c_{Re}^*}{\partial t^*} &= \frac{\ell_R^2}{D_{O_2}} \left(- \left(k_{1c} + k_{1a} + k_{2a} + k_{2c} c_{O_2}^0 c_{O_2}^* \right) c_{Re}^* \right. \\ &\quad \left. + k_{1c} + k_{2a} \right) && \text{at } \Gamma_{sf} && (16e) \\ \text{I.C.1} \quad c_{O_2}^* &= 1 && \text{in } \Omega_f \cup \Omega_e \text{ at } t^* = 0 && (16f) \\ \text{I.C.2} \quad c_{Re}^* &= 0 && \text{at } \Gamma_{sf} \text{ at } t^* = 0 && (16g) \\ c_{O_2}^*(x^*, y^*, z^*) &= c_{O_2}^*(x^* + 1, y^* + 1, z^*), && \text{in } \Omega_f && (16h) \\ \mathbf{n} \cdot \nabla^* c_{O_2}^*(x^*, y^*, z^*) &= \mathbf{n} \cdot \nabla^* c_{O_2}^*(x^* + 1, y^* + 1, z^*), && \text{in } \Omega_f && (16i) \\ c_{Re}^*(x^*, y^*, z^*) &= c_{Re}^*(x^* + 1, y^* + 1, z^*), && \text{at } \Gamma_{sf} && (16j) \end{aligned}$$

191

192 Voltammetry simulation, with a scan-rate $r_E = 5 \text{ mV/s}$ and an initial potential value of
 193 0.6 V , was carried out with $L_e^* = 10$ and $L_N = 20 \text{ } \mu\text{m}$ (*i.e.* $L_N^* \simeq 12$). Values of the other
 194 physical parameters are reported in Table. 1. It should be noted that k_{2a} is taken equal to
 195 zero since the reduction of O_2 is considered as irreversible. Since BOD is the enzyme for the
 196 catalytic reaction, $n_1 = 1$ [38].

Parameter	Symbol	Value	Unit
Ideal gas constant	R	8.314	$Jmol^{-1}K^{-1}$
Faraday's constant	F	96485.33	$Cmol^{-1}$
Number of transferred electron	n_1	1	—
Electron transfer coefficient	α_1	0.5	—
Standard potential vs. $E_{Ag/AgCl}^0$	$E_{Ox/Re}^0$	0.41	V
Equilibrium potential vs. $E_{Ag/AgCl}^0$	E_{O_2/H_2O}	0.619	V
Scan rate	r_E	5	mVs^{-1}
Temperature	T	298	K
Bulk concentration	$c_{O_2}^0$	1.2	$mol\ m^{-3}$
Total surface concentration of enzymes	c_E^t	10^{-8}	$mol\ m^{-2}$
Diffusion coefficient	\mathcal{D}_{O_2}	$2 \cdot 10^{-9}$	m^2s^{-1}
Standard rate constant	k_0	10	s^{-1}
Electron transfer rate constant	k_{2c}	485.83	$m^3mol^{-1}s^{-1}$
Spherical pore diameter	d_s	1.17	μm
Relative pore connection window size	d_c/d_s	15%	—
Size of the periodic unit cell	ℓ_R	1.678	μm

Table 1: Parameters used for the simulations

197 The software COMSOL Multiphysics (ver. 5.4), with physics-controlled mesh including
 198 extremely fine grid blocks composed of 10^7 tetrahedral elements in the overall domain, was
 199 used to solve this problem. The typical computational time is about 12 hours on a Dell
 200 PowerEdge 430 - 2 processors Intel Xeon E5-2630v3.

201 Dimensionless oxygen concentration fields obtained from DNS in Ω_f and Ω_e are repre-
 202 sented in Fig. 4 at $t = 10\ s, 55\ s$ and $70\ s$, highlighting the coupled diffusion-reaction process
 203 inside the porous electrode and showing the oxygen concentration decrease with time. In
 204 this configuration, $Ki = 10^{-3}$, a value that satisfies the constraint in (10a).

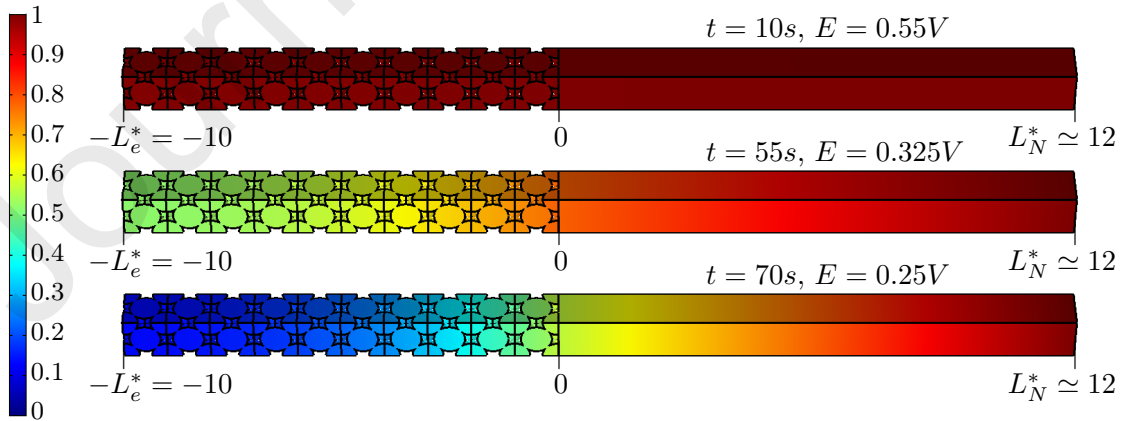


Figure 4: Normalized O_2 concentration fields, $c_{O_2}^*$, at $t = 10\ s, 55\ s$ and $70\ s$, the corresponding potential values being $E = 0.55\ V, 0.325\ V$ and $E = 0.25\ V$, respectively.

205 These results can now be directly compared to simulations of the macroscopic model and
 206 this is the object of the following section.

207 *4.2. Solution of the macroscopic model and comparisons with DNS*

208 Our aim now is to explore the relevance of the macroscopic model, its performance to
 209 predict the average concentrations and the current delivered by the electrode. Since the FCC
 210 structure under consideration here is isotropic, $\mathbf{D}_{eff} = \mathcal{D}_{eff}\mathbf{I}$ (\mathbf{I} being the identity tensor) and
 211 the macroscopic model reduces to 1D. The macroscopic computational domain constituted
 212 by the 1D effective medium for the electrode and the diffusion layer is represented in Fig. 5.

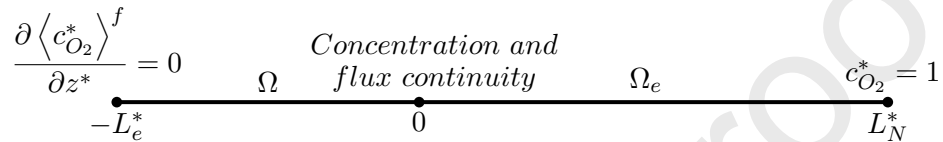


Figure 5: 1D configuration for the macroscopic numerical simulation.

213

Using the same reference quantities, the dimensionless macroscopic problem can be writ-

ten as

$$\begin{aligned} \varepsilon_f \frac{\partial \langle c_{O_2}^* \rangle^f}{\partial t^*} &= \varepsilon_f \mathbf{D}_{eff}^* \frac{\partial^2 \langle c_{O_2}^* \rangle^f}{\partial z^{*2}} \\ &\quad - \frac{a_v \ell_R^2 c_E^t}{\mathcal{D}_{O_2} c_{O_2}^0} \left(k_{2c} c_{O_2}^0 \langle c_{O_2}^* \rangle^f \langle c_{Re}^* \rangle_{sf} \right. \\ &\quad \left. + k_{2a} \left(\langle c_{Re}^* \rangle_{sf} - 1 \right) \right) \quad \text{in } \Omega \quad (17a) \end{aligned}$$

$$\begin{aligned} \frac{\partial \langle c_{Re}^* \rangle_{sf}}{\partial t^*} &= \frac{\ell_R^2}{\mathcal{D}_{O_2}} \left(-(k_{1c} + k_{1a} + k_{2a}) \langle c_{Re}^* \rangle_{sf} \right. \\ &\quad \left. - k_{2c} c_{O_2}^0 \langle c_{O_2}^* \rangle^f \langle c_{Re}^* \rangle_{sf} + k_{1c} + k_{2a} \right) \quad \text{in } \Omega \quad (17b) \end{aligned}$$

$$\text{B.C.1} \quad \langle c_{O_2}^* \rangle^f = c_{O_2}^* \quad \text{at } z^* = 0 \quad (17c)$$

$$\text{B.C.2} \quad \varepsilon_f \mathbf{D}_{eff}^* \frac{\partial \langle c_{O_2}^* \rangle^f}{\partial z^*} = \frac{\partial c_{O_2}^*}{\partial z^*} \quad \text{at } z^* = 0 \quad (17d)$$

$$\frac{\partial c_{O_2}^*}{\partial t^*} = \frac{\partial^2 c_{O_2}^*}{\partial z^{*2}} \quad \text{in } \Omega_e \quad (17e)$$

$$\text{B.C.3} \quad \frac{\partial \langle c_{O_2}^* \rangle^f}{\partial z^*} = 0 \quad \text{at } z^* = -L_e^* \quad (17f)$$

$$\text{B.C.4} \quad c_{O_2}^* = 1 \quad \text{at } z^* = L_N^* \quad (17g)$$

$$\text{I.C. 1} \quad \langle c_{O_2}^* \rangle^f = 1 \quad \text{in } \Omega \text{ at } t^* = 0 \quad (17h)$$

$$\text{I.C. 2} \quad \langle c_{Re}^* \rangle_{sf} = 0 \quad \text{in } \Omega \text{ at } t^* = 0 \quad (17i)$$

$$\text{I.C. 3} \quad c_{O_2}^* = 1 \quad \text{in } \Omega_e \text{ at } t^* = 0 \quad (17j)$$

214 In Eq. (17a), \mathbf{D}_{eff}^* represents the dimensionless effective diffusion coefficient, $\mathbf{D}_{eff}^* =$
 215 $\mathbf{D}_{eff}/\mathcal{D}_{O_2}$. Prior to the solution of the above model, the closure problem in Eqs. (13)
 216 was solved over a periodic FCC unit cell. Both the closure and macroscopic problems were
 217 solved with COMSOL Multiphysics (ver. 5.4).

218 Voltammetry simulation using the 1D-macroscopic effective model in Eqs (17) was car-
 219 ried out in the same conditions as for the 3D DNS at the microscale presented in Section
 220 4.1, *i.e.* using the parameters indicated in Table 1 with $L_e^* = 10$ and $L_N^* \simeq 12$. For this mi-
 221 crostructure, $\varepsilon_f = 0.763$, $a_v^* = 5.985$ and $\varepsilon_f \mathbf{D}_{eff}^* = 0.364$. The mesh used for this simulation
 222 is made of ~ 800 elements. The pore-scale fields of $c_{O_2}^*$ and c_{Re}^* were averaged in each unit
 223 cell over \mathbf{V}_f and \mathbf{A}_{sf} respectively and then compared to $\langle c_{O_2}^* \rangle^f$ and $\langle c_{Re}^* \rangle_{sf}$ obtained from
 224 the solution of the macroscopic model.

225 The dimensionless oxygen concentration profiles inside the porous electrode, obtained
 226 from the 3D-DNS and 1D simulation, are represented at the three times $t = 10$ s, 55 s and
 227 70 s in Fig. 6. This concentration decreases with time as a result of the reduction reaction
 228 while its gradient increases at the electrode-diffusion layer interface ($z^* = 0$) and hence

229 inside the electrode. As shown on this figure, the agreement between the two approaches is
 230 excellent.

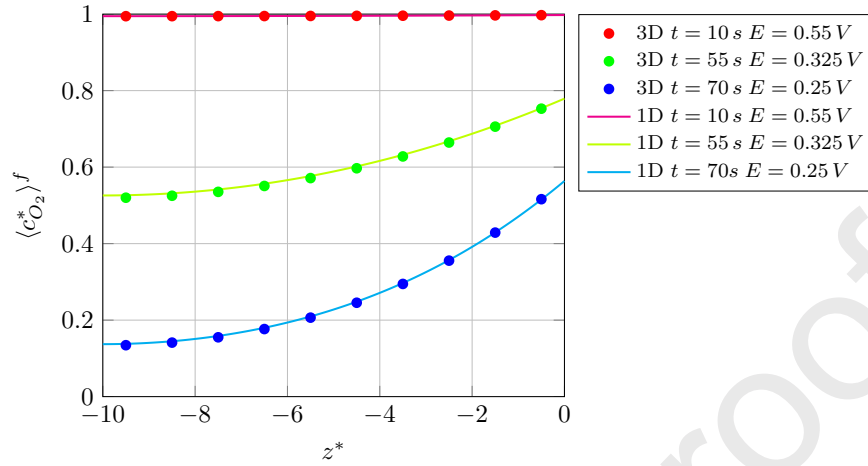


Figure 6: Comparison of the concentration profiles of oxygen obtained from the 3D DNS (micromodel) and 1D (macromodel) simulation. All the data employed to carry out both the pore-scale DNS and the macroscale simulation are mentioned in the text above and in Table 1.

231 Similarly, the dimensionless reduced enzyme surface concentration profiles obtained with
 232 both the micro and macro-scale models are reported in Fig. 7. Again, the comparison
 233 between the two shows an excellent agreement, confirming the validity of the new macroscopic
 234 model derived in this work.

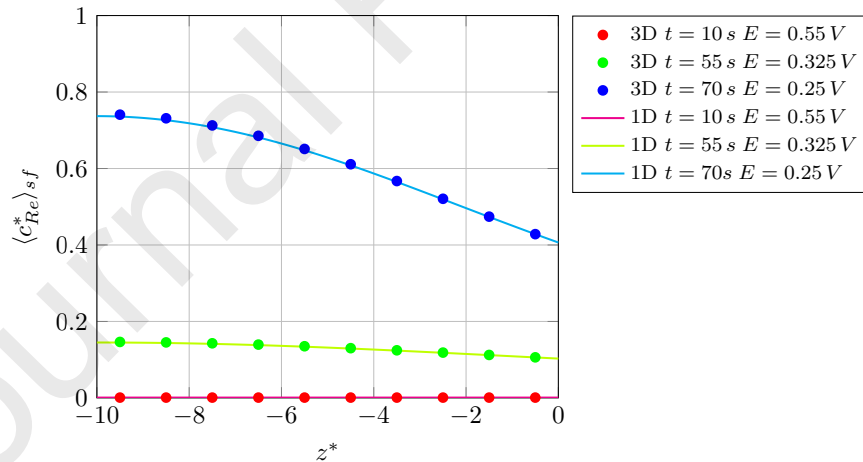


Figure 7: Comparison of reduced enzyme concentration profiles obtained from the 3D DNS (micromodel) and 1D (macromodel) simulation.

235 As a final important check, the interest must now be focused on the current curves
 236 in voltamograms. The current was computed by making use of Eqs. (6) and (7) in the
 237 microscale approach and with Eqs. (14) and (15) involving the average reduced enzyme
 238 concentration obtained from the solution of the macroscopic model. In Fig. 8, the current

239 per unit cross-sectional area of the electrode is represented versus the scanning potential
 240 ranging from 0.6 V to 0.1 V. A special attention must be dedicated to the mesh refinement
 241 for the 3D DNS in COMSOL Multiphysics. A tetrahedral mesh made of $\sim 3.3 \times 10^5$ elements
 242 for the domain under consideration in Fig. 3 was used to obtain converged results. As can
 243 be seen in Fig. 8, the agreement between the two approaches is again excellent.

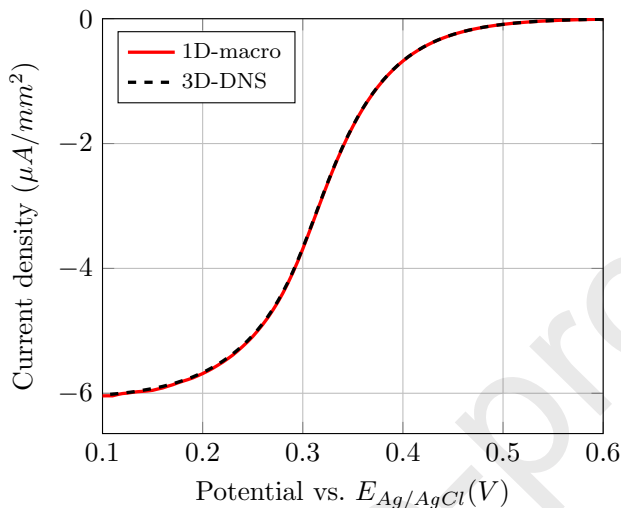


Figure 8: Comparison between the current per unit electrode cross-sectional area versus the scanning potential during voltammetry obtained from the 3D DNS and 1D macroscopic model.

244 This again confirms the perfect agreement between the two approaches and completes
 245 the validation of the new macroscopic model which provides a powerful tool to predict the
 246 macroscopic behavior of a porous electrode operating in the DET mode. In addition it must
 247 be emphasized that this original macroscopic approach allows a considerable computational
 248 speedup. Indeed, in the case under consideration in this section, the macroscale solution
 249 requires only 4 seconds, which, compared to the corresponding 3D DNS with the above
 250 mentioned mesh (85 minutes), represents a speedup of about 1300.

251 In the following section, the ability of the macroscopic model to predict the current-to-
 252 potential relationship characteristics of an electrode is reported through comparisons with
 253 experimental voltammetry results obtained with a porous gold electrode coated with BOD
 254 as the bioelectrocatalyst at the cathode.

255 5. Comparison with experimental data

256 In this section, the capability of the macroscopic model to predict voltammetry experi-
 257 mental data is investigated. To this purpose, experiments were carried out on porous gold
 258 electrodes.

259 5.1. Experimental details

260 The three main steps of the experimental protocol consist in the electrode synthesis, the
 261 enzyme immobilization and the electrocatalytic characterization.

Electrode Synthesis

Cylindrical macroporous gold electrodes were prepared using a Langmuir-Blodgett technique as shortly described in the introduction and detailed in [2, 8, 9]. In brief, silica beads with a diameter of 1170 nm ($d_s = 1.2 \mu\text{m}$ is taken as an accurate enough value) were spread from an ethanol/chloroform (20% v/v-80% v/v) suspension at the water-air interface of a Langmuir-Blodgett trough. An optimal monolayer of silica beads was obtained at the water-air interface after compression by closing the moveable barriers. Then, multiple silica particle layers were transferred onto gold wires of 250 μm in diameter and 4 cm in length. This was achieved by repeating the dipping and withdrawing process at a speed of 1.2 mm/min. After the formation of the silica template layers on the surface, Elevate[®] Gold 7990 was used for the gold electrodeposition over a length of 2 cm by applying a constant potential of -0.6 V. The number of macroporous layers is controlled by following the current oscillations. After dissolving the silica particles in 5% hydrofluoric acid for several minutes, the final macroporous gold electrode is obtained as an inverse opale gold structure. Four electrodes were prepared, having 3, 7, 11 and 19 half-layers (HL) of pores. At this stage, the internal pore surfaces were coated with a genetically engineered variant of Bilirubin oxidase from *M. oryzae* whose serine in position 362 was replaced by a cysteine (BOD S362C) [52]. This was performed over the porous zone being 2 cm long, corresponding to a surface area of the initial wire of 15 mm². The actual active surface area depends on the thickness of the porous layers of the electrode. There is a linear correspondence between the active area of the porous electrode and the number of porous half layers, as reported recently [53].

Enzyme Immobilization

A 0.1 mM BOD S362C ($516 \pm 38 \text{ U/mg}$) solution was prepared in 50 mM phosphate buffer (pH 6.0). Since the cysteine residue on the outer surface of bilirubin oxidase is close to the T1 active center, the interaction between the thiol group on the cysteine residue and the gold surface allows the formation of a self-assembled monolayer of BOD S362Cs on the internal surface of the pores. This allows a proper orientation of the BOD on the electrode surface and favors the interfacial electron transfer. The macroporous gold electrode was dipped into the enzyme solution after being treated with plasma for 15 min. Vacuum was then applied for 3 min to ensure an efficient penetration of enzymes into the whole porous structure. The electrode was kept at 4 °C overnight. After rinsing with distilled water and with 0.1 M PBS pH 7.2 under stirring, the electroenzymatic O_2 reduction was performed with the BOD modified electrodes.

Electrocatalytic characterization

All electrochemical measurements were performed with an Autolab PGSTAT101 potentiostat monitored by a PC running Nova 1.6. A Ag/AgCl (3 M KCl) was used as a reference electrode, and a cylindrical carbon sheet was employed as an auxiliary electrode. For the electrochemical reduction, the buffer solution was purged with O_2 for 15 min. Then, the electrodes were dipped into the buffer solution maintained at ambient temperature while a slow flow of O_2 was kept above it inside a sealed cell for the O_2 concentration to remain constant in the buffer. Voltammetry experiments were carried out in the potential range from 0.6 V to 0.15 V with a scan rate of 5 mV/s. The temperature was 25 °C for these

304 experiments. Each experiments was at least performed in triplicate.

305 5.2. Voltammetry interpretation

306 The templating procedure leads to a rather compact bead arrangement so that an FCC
 307 periodic cell represents a reasonable model for the resulting structure. This was observed
 308 in the work reported in [9] and further confirmed in a recent in-depth analysis of the 3D
 309 microstructure extracted from FIB-SEM imaging [54]. The relative size of the pore connec-
 310 tion window, d_c/d_s was taken equal to 15%, which can be considered as the minimum value
 311 for this manufacturing process [55]. With these structural parameters, the effective diffusion
 312 coefficient was computed to be $\varepsilon_f D_{eff}^* = 0.364$.

313 Interpretation of the experimental voltammetry data is carried out using a fitting pro-
 314 cedure on some of the parameters involved in the macroscale model in Eqs. (17) that are
 315 unknown a priori. To do so, k_0 , k_{2c} , α_1 and $E_{Ox/re}^0$ were estimated using a fitting procedure
 316 in the least square sense on data obtained with the 11HL electrode. It must be reminded
 317 that the individual values of n_2 and α_2 are not required and that k_{2a} is taken equal to zero
 318 in agreement with the irreversibility of oxygen reduction¹. The fitted resulting values are
 319 reported in Table 2 and were kept the same to predict the voltammetry results on the other
 320 electrodes.

k_0 (s^{-1})	k_{2c} ($m^3 mol^{-1} s^{-1}$)	α_1 (-)	$E_{Ox/Re}^0$ (V)
10.5	25.9	0.46	0.405

Table 2: Parameters fitted on the voltammetry results obtained with the 11HL electrode and used for all the other predictions employing the macroscopic model.

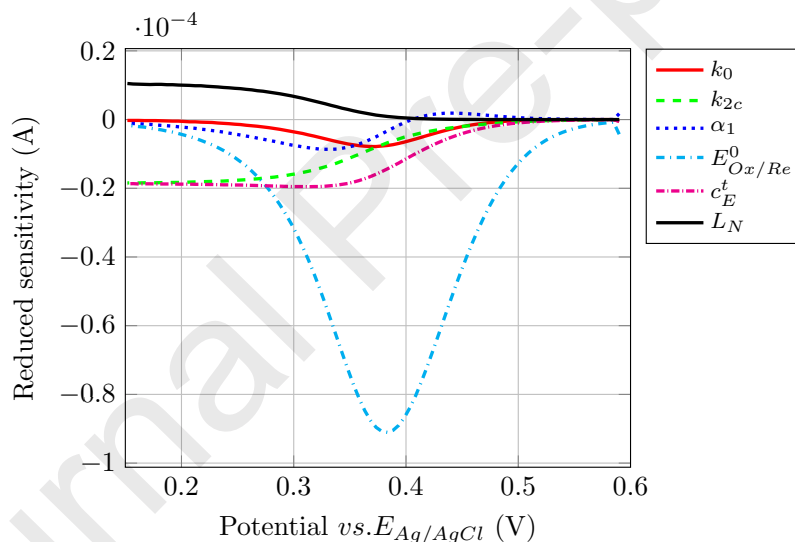
321 Moreover, the total concentration of enzyme, c_E^t , and the diffusion layer thickness, L_N ,
 322 that are subject to vary from one electrode to another, were fitted for each corresponding
 323 experimental data set. In fact, the diffusion layer thickness depends on the rate of oxygen
 324 depletion within the fluid in contact with the outer interface of the electrode, and this
 325 rate depends itself on the electrode thickness. Here, a simplified approach is adopted by
 326 considering L_N as constant which means that this parameter should be understood as a mean
 327 value over the period of potential scanning for each experiment. The values are indicated in
 328 Table 3; those for the remaining parameters are given in Table 1. It should be noted that
 329 the total enzyme surface concentration slightly decreases with the electrode thickness and
 330 this can be explained by the fact that, the thicker the porous material, the more difficult is
 331 the penetration of enzyme during the coating process deeper in the pores far from the free
 332 surface of the electrode. This observation was also part of the conclusions in the work by
 333 Do *et al.* [42] on a somewhat different system.

¹The value of k_{2a} was also identified in the fitting procedure and showed to be so small that it is insensitive in the current response.

Electrodes	3HL	7HL	11HL	19HL
c_E^t ($mol\ m^{-2}$)	8.9×10^{-8}	8.07×10^{-8}	5.7×10^{-8}	4.06×10^{-8}
L_N (μm)	186	158	59	44

Table 3: Parameters used in the simulations for the fits.

334 To assess the validity of the identification procedure, a sensitivity analysis of the current
335 to all the fitted parameters was performed. The reduced sensitivity to a parameter, u , is
336 defined as $u\partial I/\partial u$, u being either k_0 , k_{2c} , α_1 , $E_{Ox/Re}^0$, L_N or c_E^t here. It was computed using
337 the 1D macroscopic model at the nominal values of each parameter identified on the 11HL
338 electrode. Sensitivities to all the parameters are represented versus the scanning potential
339 in the interval of interest in Fig. 9. This figure clearly shows that all the sensitivities
340 are significantly larger than the precision of the potentiostat used to measure the current
341 which can be estimated to be less than $0.02 \cdot 10^{-5}$ A over a very wide potential interval. In
342 addition, the sensitivities are not proportional to each other, ensuring that parameters are
343 uncorrelated. This analysis indicates that the identification procedure is robust and reliable.

Figure 9: Reduced sensitivities of the current to the parameters k_0 , k_{2c} , α_1 , $E_{Ox/Re}^0$, L_N and c_E^t at their identified values on the 11HL electrode versus the scanning potential.

344 The current versus the scanning potential obtained from our numerical simulation is
345 represented in Fig. 10 together with the experimental results. As can be seen from this
346 figure, excellent agreement is obtained for all the electrodes tested in this work over the
347 whole scanned potential interval. In this potential interval, oxygen reduction on unmodified
348 gold electrodes is not observed, because this reaction starts to occur only for potentials more
349 negative than 0.1 V vs $Ag/AgCl$. Therefore, the signals should not be disturbed by such an
350 eventual interference.

351 The experimental measurements show a slight crossover of the current signals at large
 352 potentials for the thickest electrodes (11HL and 19HL). A possible explanation of this behav-
 353 ior might be that, at the very beginning of the bioelectrocatalytic reaction (onset potential
 354 of around $+0.5V$), not all the enzyme modified layers are contributing immediately to the
 355 catalytic current for these two electrodes. Preferentially the outermost layers (most likely 2-3
 356 half-layers, when looking at the relative positions of the plateau current for the 3 half-layer
 357 electrode ($15\mu A$) and the crossover current ($10\mu A$)) are involved. Therefore the measured
 358 current is smaller with respect to what it should be in the ideal case when all the porous
 359 layers are active immediately. Only at higher driving forces ($E < +0.4V$), when the enzymes
 360 in the outer layers are already turning at their maximum speed, and thus cannot convert
 361 more oxygen per time unit, the inner layers start contributing as well because the oxygen
 362 diffusion layer now also reaches the inner part of the electrode. This leads to the observed
 363 crossover that is however not reproduced by the model which would require involving a
 364 concentrations-dependent catalytic rate constant. This effect is nevertheless of very weak
 365 importance.

366 The absolute value of the relative error between the two, taking the experimental data as
 367 the reference, is less than 5% as shown in Fig. 11 and is distributed around 0. It remains even
 368 smaller than 3.5% when the potential is less than $\sim 0.37V$ for all the electrodes. Moreover,
 369 the relative error when repeating several times the experiments is very small. For example,
 370 preparing three 7HL electrodes leads to electrocatalytic currents with a standard deviation
 371 of $0.08 \cdot 10^{-5} A$.

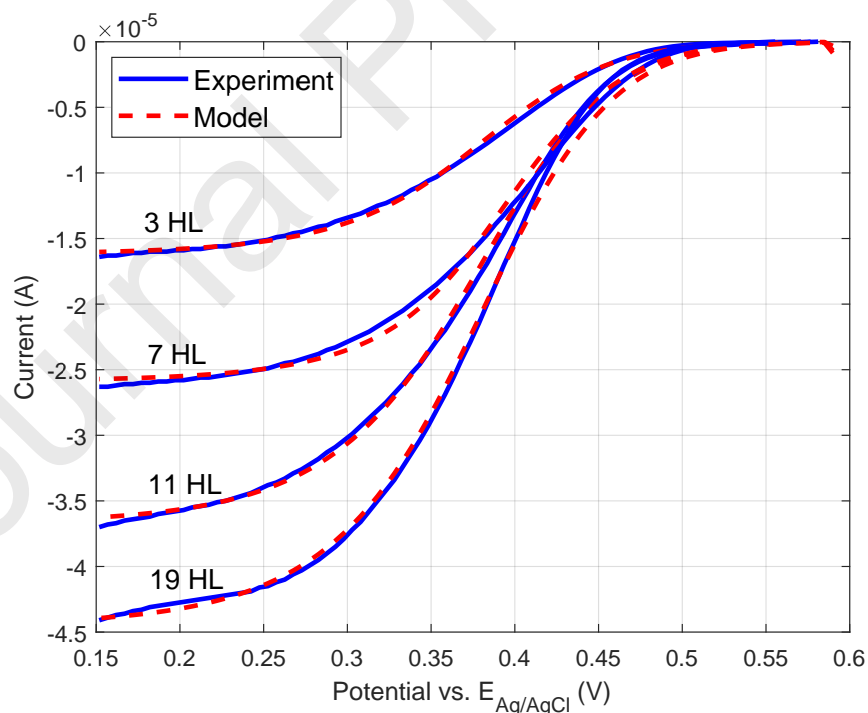


Figure 10: Current versus the scanning potential obtained from voltammetry numerical simulations using the macroscopic model. Comparison with the experimental data.

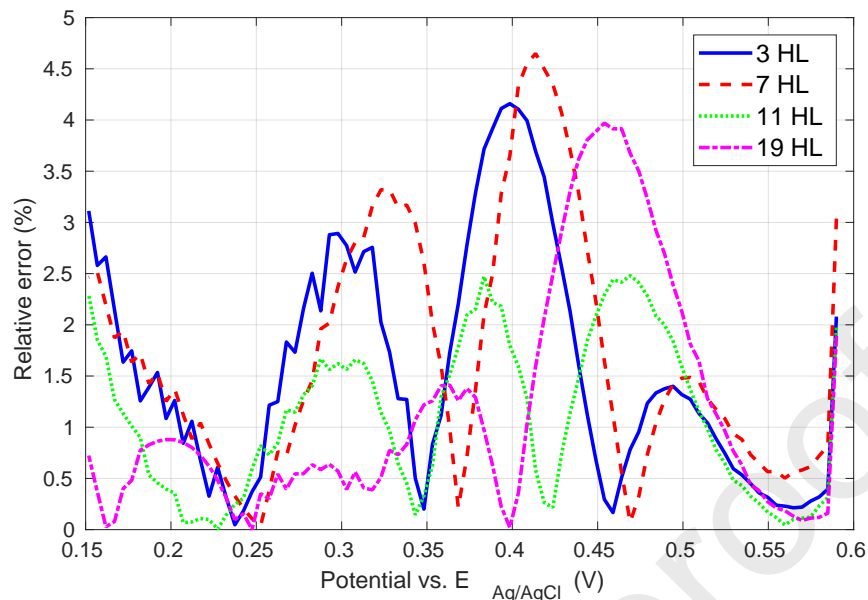


Figure 11: Absolute value of the relative error on the current estimated from the macroscopic model and obtained from experimental voltammetry data, taking the latter as the reference.

372 This successful comparison represents a strong validation step of the new macroscopic
 373 model derived in this work, assessing its relevance and performance to reproduce the physico-
 374 electrochemical behavior of the porous electrodes operating in the DET mode.

375 6. Conclusions

376 In this work, a new multiscale modelling for diffusion and electrochemical enzymatic
 377 reaction involved in a porous electrode operating in the DET mode was developed. The
 378 unsteady pore-scale model was provided for oxygen reduction taking into account the electron
 379 transfer process at play. An upscaling procedure, in which coupling and non-linearities were
 380 handled, was applied to obtain a closed unsteady macroscopic model valid at the electrode
 381 scale. The associate closure problem yielding the effective diffusivity tensor was provided.
 382 This approach represents an original macroscopic model that has not been reported so far in
 383 the literature. In particular, unsteadiness, which has been disregarded in existing models for
 384 enzymatic porous electrodes, was explicitly taken into account. Moreover coupling between
 385 mass transport and enzymatic reaction in a non-linear way has been carried out through
 386 the upscaling procedure. This yields new terms induced by the enzymatic reaction in the
 387 macroscopic mass conservation equations (for enzyme and oxygen). Both the micro- and
 388 macroscale models were further used in the case of oxygen reduction in the presence of BOD
 389 as a catalyst. The successful comparison of numerical voltammetry simulations, carried
 390 out on a porous model structure with the 3D pore-scale model and the macroscale model
 391 which reduces to 1D, assessed the validity of the latter. This macroscopic model was further
 392 employed to predict experimental voltammetry results obtained with porous gold electrodes
 393 coated with BOD. The excellent prediction confirms the relevance of the approach and the

394 validity of this macroscopic model which provides an efficient tool operational at the electrode
 395 scale, allowing a considerable computational speedup. In particular, this model allows one to
 396 efficiently carry out a sensitivity analysis, which provides important indications on the most
 397 significant parameters involved in the physico-electrochemical process, a task that would be
 398 otherwise extremely cumbersome to perform with the pore-scale model. It also provides a
 399 mean to estimate parameters that are involved in the experiment (as for example the total
 400 enzyme concentration and standard rate constants). It could also be employed to interpret
 401 electrochemical impedance spectroscopy tests on electrodes for which dynamic effects are
 402 expected. More importantly, this model represents an essential tool for a rational optimal
 403 design of enzymatic porous electrodes. The multiscale approach developed here represents a
 404 breakthrough and could be widely used for other electrochemical processes in porous media.

405 **Acknowledgement**

406 This work was supported by the LabEx AMADEus (ANR-10-LABX-42) within IdEx
 407 Bordeaux (ANR-10-IDEX-03-02), *i.e.* the Investissements dAvenir Programme of the French
 408 government managed by the Agence Nationale de la Recherche (ANR). It also benefited from
 409 the support of the ANR projects MOMA (ANR-17-CE08-0005) and BIO3 (ANR- 16-CE19-
 410 0001). This project has also received partial funding from the European Unions Horizon 2020
 411 research and innovation programme under the Marie Skodowska-Curie grant agreement No
 412 813006.

413 **Appendix A Volume averaging and derivation of the upscaled model**

414 In this Appendix, the upscaling procedure to derive the macroscopic diffusion/reaction
 415 equation by volume averaging the microscopic initial boundary value problem (IBVP) in
 416 Eqs. (5) is detailed. Volume averaging is applied according to the following four main steps
 417 (see Chap. 1 in [45] and [56]) and c_{O_2} is used to denote $c_{O_2}(\mathbf{r}, t)$.

418 **Step 1:** *Application of the superficial averaging operator*

419 The superficial and area averages are defined as

$$\begin{aligned} \langle f \rangle |_{\mathbf{x}} &= \frac{1}{V} \int_{V_f(\mathbf{x})} f|_{\mathbf{x}+\mathbf{y}} dV \\ \langle f \rangle_{sf} |_{\mathbf{x}} &= \frac{1}{A_{sf}} \int_{A_{sf}(\mathbf{x})} f|_{\mathbf{x}+\mathbf{y}} dA \end{aligned} \quad (\text{A.1})$$

420 The superficial average operator is applied to the microscale IBVP and, with the purpose of
 421 deriving a model involving averages only, time and spatial derivation must be interchanged
 422 with volume averaging. This is achieved by using the general transport theorem, which,
 423 since the averaging volume is fixed in time and the porous medium is rigid, reduces in the
 424 present case to

$$\left\langle \frac{\partial f}{\partial t} \right\rangle = \frac{\partial \langle f \rangle}{\partial t} \quad (\text{A.2})$$

425 and the spatial averaging theorem (or Leibnitz rule) given by [45, 57]

$$\langle \nabla f \rangle = \nabla \langle f \rangle + \frac{1}{V} \int_{\mathbf{A}_{sf}} \mathbf{n} f dA \quad (\text{A.3})$$

426 together with a straightforward similar form for the divergence operator.

427 With this at hand, the superficial average can be applied to the mass balance equation
 428 (5d) for O_2 and, employing the boundary condition at \mathbf{A}_{sf} , one arrives at the following
 429 average form

$$\begin{aligned} \varepsilon_f \frac{\partial \langle c_{O_2} \rangle^f}{\partial t} = & \nabla \cdot \left[\mathcal{D}_{O_2} \left(\varepsilon_f \nabla \langle c_{O_2} \rangle^f + \langle c_{O_2} \rangle^f \nabla \varepsilon_f + \frac{1}{V} \int_{\mathbf{A}_{sf}} \mathbf{n} c_{O_2} dA \right) \right] \\ & - k_{2c} a_v \langle c_{O_2} c_{Re} \rangle_{sf} - k_{2a} a_v \langle c_{Re} \rangle_{sf} + k_{2a} a_v c_E^t \end{aligned} \quad (\text{A.4})$$

430 where the intrinsic average concentration was used instead of the superficial average.

431 **Step 2:** *Decomposition of c_{O_2} and simplifications due to length-scale constraints*

The averaged equation (A.4) contains both average and point-wise concentrations. To remove the latter, the spatial decomposition

$$c_{O_2} = \langle c_{O_2} \rangle^f + \tilde{c}_{O_2} \quad (\text{A.5})$$

is introduced [58], where \tilde{c}_{O_2} is the deviation of concentration which fluctuates at a typical length-scale ℓ_p while $\langle c_{O_2} \rangle^f$ experiences significant variations at the scale L . It should be noted that a consequence of this decomposition is $\langle \tilde{c}_{O_2} \rangle^f = 0$, taking into account the scale hierarchy $\ell_p \ll L$. When this decomposition is inserted into Eq. (A.4), one gets

$$\begin{aligned} \varepsilon_f \frac{\partial \langle c_{O_2} \rangle^f}{\partial t} = & \nabla \cdot \left[\mathcal{D}_{O_2} \left(\varepsilon_f \nabla \langle c_{O_2} \rangle^f + \langle c_{O_2} \rangle^f \nabla \varepsilon_f + \frac{1}{V} \int_{\mathbf{A}_{sf}} \mathbf{n} \langle c_{O_2} \rangle^f dA \right. \right. \\ & \left. \left. + \frac{1}{V} \int_{\mathbf{A}_{sf}} \mathbf{n} \tilde{c}_{O_2} dA \right) \right] - k_{2c} a_v \langle c_{O_2} c_{Re} \rangle_{sf} - k_{2a} a_v \langle c_{Re} \rangle_{sf} + k_{2a} a_v c_E^t \end{aligned} \quad (\text{A.6})$$

Attention must now be paid to the area integral term $\frac{1}{V} \int_{\mathbf{A}_{sf}} \mathbf{n} \langle c_{O_2} \rangle^f dA$ on the right hand side of Eq. (A.6). This term must be evaluated at the centroid \mathbf{x} of the averaging volume V and requires first the evaluation of $\langle c_{O_2} \rangle^f$ at any point $\mathbf{x} + \mathbf{y}$ on \mathbf{A}_{sf} contained in V , making this term non-local. A Taylor expansion given by

$$\langle c_{O_2} \rangle^f |_{\mathbf{x}+\mathbf{y}} = \langle c_{O_2} \rangle^f |_{\mathbf{x}} + \mathbf{y} \cdot \nabla \langle c_{O_2} \rangle^f |_{\mathbf{x}} + \frac{1}{2} \mathbf{y} \mathbf{y} : \nabla \nabla \langle c_{O_2} \rangle^f |_{\mathbf{x}} + \dots \quad (\text{A.7})$$

may be employed and, when introduced back into Eq. (A.6) together with the fact that

$$\frac{1}{V} \int_{\mathbf{A}_{fs}} \mathbf{n} dA = -\nabla \langle 1 \rangle = -\nabla \varepsilon_f \quad (\text{A.8})$$

$$\frac{1}{V} \int_{\mathbf{A}_{fs}} \mathbf{n} \mathbf{y} dA = -\nabla \langle \mathbf{y} \rangle \quad (\text{A.9})$$

$$\frac{1}{V} \int_{\mathbf{A}_{fs}} \mathbf{n} \mathbf{y} \mathbf{y} dA = -\nabla \langle \mathbf{y} \mathbf{y} \rangle \quad (\text{A.10})$$

the average form of the mass conservation equation of species A takes the form

$$\begin{aligned} \varepsilon_f \frac{\partial \langle c_{O_2} \rangle^f}{\partial t} = & \nabla \cdot \left[\mathcal{D}_{O_2} \left(\varepsilon_f \nabla \langle c_{O_2} \rangle^f - \nabla \langle \mathbf{y} \rangle \cdot \nabla \langle c_{O_2} \rangle^f \right. \right. \\ & \left. \left. - \frac{1}{2} \nabla \langle \mathbf{y} \mathbf{y} \rangle : \nabla \nabla \langle c_{O_2} \rangle^f - \dots + \frac{1}{V} \int_{\mathbf{A}_{sf}} \mathbf{n} \tilde{c}_{O_2} dA \right) \right] \\ & - k_{2c} a_v \langle c_{O_2} c_{Re} \rangle_{sf} - k_{2a} a_v \langle c_{Re} \rangle_{sf} + k_{2a} a_v c_E^t \end{aligned} \quad (\text{A.11})$$

With the purpose of simplifying this last equation, orders of magnitude can be employed to determine the important contributions among all the diffusive terms. Indeed, the following estimates can be derived

$$\varepsilon_f \nabla \langle c_{O_2} \rangle^f = \mathbf{O} \left(\varepsilon_f \frac{\langle c_{O_2} \rangle^f}{L} \right) \quad (\text{A.12a})$$

$$\nabla \langle \mathbf{y} \rangle \cdot \nabla \langle c_{O_2} \rangle^f = \mathbf{O} \left(\frac{\varepsilon_f r_0}{L} \frac{\langle c_{O_2} \rangle^f}{L} \right) \quad (\text{A.12b})$$

$$\nabla \langle \mathbf{y} \mathbf{y} \rangle : \nabla \nabla \langle c_{O_2} \rangle^f = \mathbf{O} \left(\left(\frac{\varepsilon_f r_0}{L} \right)^2 \frac{\langle c_{O_2} \rangle^f}{L} \right) \quad (\text{A.12c})$$

On the basis of the scale hierarchy, it is not hard to deduce that Eq. (A.11) can be simplified to

$$\begin{aligned} \varepsilon_f \frac{\partial \langle c_{O_2} \rangle^f}{\partial t} = & \nabla \cdot \left[\mathcal{D}_{O_2} \left(\varepsilon_f \nabla \langle c_{O_2} \rangle^f + \frac{1}{V} \int_{\mathbf{A}_{sf}} \mathbf{n} \tilde{c}_{O_2} dA \right) \right] \\ & - k_{2c} a_v \langle c_{O_2} c_{Re} \rangle_{sf} - k_{2a} a_v \langle c_{Re} \rangle_{sf} + k_{2a} a_v c_E^t \end{aligned} \quad (\text{A.13})$$

In order to progress to a form of this last expression involving $\langle c_{O_2} \rangle^f$ only, the order of magnitude of \tilde{c}_{O_2} shall be obtained in comparison to that of $\langle c_{O_2} \rangle^f$. To do so, B.C. 1 in Eq; (5e) can be rewritten as

$$-\mathbf{n} \cdot \mathcal{D}_{O_2} \nabla \tilde{c}_{O_2} - k_{2c} \tilde{c}_{O_2} c_{Re} = \mathbf{n} \cdot \mathcal{D}_{O_2} \nabla \langle c_{O_2} \rangle^f + k_{2c} \langle c_{O_2} \rangle^f c_{Re} + k_{2a} c_{Re} - k_{2a} c_E^t \quad (\text{A.14})$$

Orders of magnitude of the deviation and average normal fluxes at \mathbf{A}_{sf} can be estimated as

$$\mathbf{n} \cdot \mathcal{D}_{O_2} \nabla \tilde{c}_{O_2} = \mathbf{O} (\mathcal{D}_{O_2} \tilde{c}_{O_2} / \ell_p) \quad (\text{A.15})$$

$$\mathbf{n} \cdot \mathcal{D}_{O_2} \nabla \langle c_{O_2} \rangle^f = \mathbf{O} (\mathcal{D}_{O_2} \langle c_{O_2} \rangle^f / L) \quad (\text{A.16})$$

This can be used in Eq. (A.14) to obtain an order of magnitude estimate of \tilde{c}_{O_2} given by

$$\tilde{c}_{O_2} = \mathbf{O} \left(\frac{(\ell_p / L) \langle c_{O_2} \rangle^f}{1 + \mathbf{O} (k_{2c} \ell_p c_{Re} / \mathcal{D}_{O_2})}, \frac{(k_{2c} \ell_p c_{Re} / \mathcal{D}_{O_2}) \langle c_{O_2} \rangle^f}{1 + \mathbf{O} (k_{2c} \ell_p c_{Re} / \mathcal{D}_{O_2})}, \frac{(k_{2a} \ell_p c_E^t / \mathcal{D}_{O_2})}{1 + \mathbf{O} (k_{2c} \ell_p c_{Re} / \mathcal{D}_{O_2})} \right) \quad (\text{A.17})$$

Noticing that $k_{2a} \ll k_{2c}$ and from the above estimate, it can be clearly seen that if the kinetic number, Ki is such that

$$Ki = \frac{k_{2c} \ell_p c_E^t}{\mathcal{D}_{O_2}} \ll 1 \quad (\text{A.18})$$

then $\tilde{c}_{O_2} \ll \langle c_{O_2} \rangle^f$ at \mathbf{A}_{sf} . Under these circumstances, Eq. (A.13) can be simplified to the following form

$$\begin{aligned} \varepsilon_f \frac{\partial \langle c_{O_2} \rangle^f}{\partial t} = & \nabla \cdot \left[\mathcal{D}_{O_2} \left(\varepsilon_f \nabla \langle c_{O_2} \rangle^f + \frac{1}{V} \int_{\mathbf{A}_{sf}} \mathbf{n} \tilde{c}_{O_2} dA \right) \right] \\ & - k_{2c} a_v \langle \langle c_{O_2} \rangle^f c_{Re} \rangle_{sf} - k_{2a} a_v \langle c_{Re} \rangle_{sf} + k_{2a} a_v c_E^t \end{aligned} \quad (\text{A.19})$$

In this equation, a close attention needs to be dedicated to the first of the three reactions terms which involves a non-local area integral. When the Taylor expansion of Eq. (A.7) is introduced in this integral, it comes

$$\langle \langle c_{O_2} \rangle^f c_{Re} \rangle_{sf} = \langle c_{Re} \rangle_{sf} \langle c_{O_2} \rangle^f |_{\mathbf{x}} + \langle \mathbf{y} c_{Re} \rangle_{sf} \cdot \nabla \langle c_{O_2} \rangle^f |_{\mathbf{x}} + \frac{1}{2} \langle \mathbf{y} \mathbf{y} c_{Re} \rangle_{sf} : \nabla \nabla \langle c_{O_2} \rangle^f |_{\mathbf{x}} + \dots \quad (\text{A.20})$$

432 For the second and third terms on the right hand side, the following estimates can be made

$$\langle \mathbf{y} c_{Re} \rangle_{sf} \ll r_0 \langle c_{Re} \rangle_{sf} \quad (\text{A.21})$$

$$\langle \mathbf{y} \mathbf{y} c_{Re} \rangle_{sf} = r_0^2 \langle c_{Re} \rangle_{sf} \quad (\text{A.22})$$

so that

$$\langle \mathbf{y} c_{Re} \rangle_{sf} \cdot \nabla \langle c_{O_2} \rangle^f \ll \mathbf{O} \left(\frac{r_0}{L} \langle c_{O_2} \rangle^f \langle c_{Re} \rangle_{sf} \right) \ll \langle c_{O_2} \rangle^f \langle c_{Re} \rangle_{sf} \quad (\text{A.23a})$$

$$\langle \mathbf{y} \mathbf{y} c_{Re} \rangle_{sf} : \nabla \nabla \langle c_{O_2} \rangle^f = \mathbf{O} \left(\left(\frac{r_0}{L} \right)^2 \right) \langle c_{O_2} \rangle^f \langle c_{Re} \rangle_{sf} \ll \langle c_{O_2} \rangle^f \langle c_{Re} \rangle_{sf} \quad (\text{A.23b})$$

This shows that the dominant term in the expansion in Eq. (A.20) is $\langle c_{O_2} \rangle^f \langle c_{Re} \rangle_{sf}$. As a consequence the average equation (A.19) can be simplified to the following form

$$\begin{aligned} \varepsilon_f \frac{\partial \langle c_{O_2} \rangle^f}{\partial t} = & \nabla \cdot \left[\mathcal{D}_{O_2} \left(\varepsilon_f \nabla \langle c_{O_2} \rangle^f + \frac{1}{V} \int_{\mathbf{A}_{sf}} \mathbf{n} \tilde{c}_{O_2} dA \right) \right] \\ & - k_{2c} a_v \langle c_{O_2} \rangle^f \langle c_{Re} \rangle_{sf} - k_{2a} a_v \langle c_{Re} \rangle_{sf} + k_{2a} a_v c_E^t \end{aligned} \quad (\text{A.24})$$

The boundary condition at the solid-fluid interface (Eq. (A.14)) can be written as

$$-\mathbf{n} \cdot \mathcal{D}_{O_2} \nabla \tilde{c}_{O_2} = \mathbf{n} \cdot \mathcal{D}_{O_2} \nabla \langle c_{O_2} \rangle^f + k_{2c} \langle c_{O_2} \rangle^f c_{Re} + k_{2a} c_{Re} - k_{2a} c_E^t \quad (\text{A.25})$$

In addition, taking into account the above order of magnitude estimate, the averaged mass conservation equation for the enzyme is given by

$$\begin{aligned} \frac{\partial \langle c_{Re} \rangle_{sf}}{\partial t} = & - (k_{1c} + k_{1a} + k_{2a}) \langle c_{Re} \rangle_{sf} - k_{2c} \langle c_{Re} \rangle_{sf} \langle c_{O_2} \rangle^f \\ & + (k_{1c} + k_{2a}) c_E^t \end{aligned} \quad (\text{A.26})$$

433 At this stage, the model remains unclosed since \tilde{c}_{O_2} is still present in the averaged mass
434 balance equation (A.24).

435 **Step 3: Closure**

The idea is now to form an IBVP (*i.e.* a closure problem) on \tilde{c}_{O_2} which solution can be inserted into the averaged equation in order to get a closed macroscopic model. This can be achieved by subtracting Eq. (A.24) divided by ε_f and Eq. (A.26) from their corresponding pore-scale equivalents in Eqs. (5d) and (5a), respectively and by using the boundary condition under the form of equation (A.25). Moreover, since the purpose is not to solve the closure problem on the entire structure of characteristic length-scale L but, rather, on a representative unit cell of the structure of characteristic length-scale ℓ_R , the external boundary condition shall be replaced by a periodic boundary condition on \tilde{c}_{O_2} (see Chap. 1 in [45]), yielding

$$\frac{\partial \tilde{c}_R}{\partial t} = - (k_{1c} + k_{1a} + k_{2a} + k_{2c} \langle c_{O_2} \rangle^f) \tilde{c}_R - k_{2c} \tilde{c}_{O_2} \langle c_{Re} \rangle_{sf} \quad (\text{A.27a})$$

$$\begin{aligned} \frac{\partial \tilde{c}_{O_2}}{\partial t} = & \nabla \cdot (\mathcal{D}_{O_2} \nabla \tilde{c}_{O_2}) - \varepsilon_f^{-1} \mathcal{D}_{O_2} \nabla \varepsilon_f \cdot \nabla \langle c_{O_2} \rangle^f - \varepsilon_f^{-1} \nabla \cdot \left(\frac{\mathcal{D}_{O_2}}{V} \int_{\mathbf{A}_{sf}} \mathbf{n} \tilde{c}_{O_2} dA \right) \\ & + \varepsilon_f^{-1} k_{2c} a_v \langle c_{O_2} \rangle^f \langle c_{Re} \rangle_{sf} + \varepsilon_f^{-1} k_{2a} a_v (\langle c_{Re} \rangle_{sf} - c_E^t) \quad \text{in } \mathbf{V}_f \end{aligned} \quad (\text{A.27b})$$

$$-\mathbf{n} \cdot \mathcal{D}_{O_2} \nabla \tilde{c}_{O_2} = \mathbf{n} \cdot \mathcal{D}_{O_2} \nabla \langle c_{O_2} \rangle^f + k_{2c} \langle c_{O_2} \rangle^f c_{Re} + k_{2a} c_{Re} - k_{2a} c_E^t \quad \text{at } \mathbf{A}_{sf} \quad (\text{A.27c})$$

$$\tilde{c}_{O_2}(\mathbf{r}, t) = \tilde{c}_{O_2}(\mathbf{r} + \ell_R \mathbf{e}_i, t) \quad (\text{A.27d})$$

436 to which an initial condition must be added. Here \mathbf{e}_i denotes one of the unit basis vectors.
437 To obtain Eq. (A.27a), the decomposition $c_{Re} = \langle c_{Re} \rangle_{sf} + \tilde{c}_R$ was employed in conjunction
438 with the fact that $\tilde{c}_{O_2} \ll \langle c_{O_2} \rangle^f$.

To simplify this problem, the following orders of magnitude can be employed

$$\nabla \cdot (\mathcal{D}_{O_2} \nabla \tilde{c}_{O_2}) = \mathbf{O} \left(\frac{\mathcal{D}_{O_2} \tilde{c}_{O_2}}{\ell_p^2} \right) \quad (\text{A.28a})$$

$$\varepsilon_f^{-1} \nabla \cdot \left(\frac{\mathcal{D}_{O_2}}{V} \int_{\mathbf{A}_{sf}} \mathbf{n} \tilde{c}_{O_2} dA \right) = \mathbf{O} \left(\frac{\mathcal{D}_{O_2} \tilde{c}_{O_2}}{\varepsilon_f L \ell_p} \right) \quad (\text{A.28b})$$

which, based on the length-scale hierarchy, indicates that the latter term is negligible with respect to the former. Moreover, the diffusive volume source $\varepsilon_f^{-1} \mathcal{D}_{O_2} \nabla \varepsilon_f \cdot \nabla \langle c_{O_2} \rangle^f$ and of the diffusive surface source $\mathbf{n} \cdot \mathcal{D}_{O_2} \nabla \langle c_{O_2} \rangle^f$ can be compared by analyzing their respective contribution per unit volume of the porous medium. The corresponding order of magnitude estimates are given by

$$\frac{1}{V} \int_{\mathbf{V}_f} \varepsilon_f^{-1} \mathcal{D}_{O_2} \nabla \varepsilon_f \cdot \nabla \langle c_{O_2} \rangle^f dV = \mathbf{O} \left(\frac{\varepsilon_f \mathcal{D}_{O_2}}{L^2} \langle c_{O_2} \rangle^f \right) \quad (\text{A.29a})$$

$$\frac{1}{V} \int_{\mathbf{A}_{sf}} \mathbf{n} \cdot \mathcal{D}_{O_2} \nabla \langle c_{O_2} \rangle^f dA = \mathbf{O} \left(\frac{\mathcal{D}_{O_2}}{\ell_p L} \langle c_{O_2} \rangle^f \right) \quad (\text{A.29b})$$

showing that the diffusive volume source has a negligible contribution. In addition, when the process is considered at a time scale constrained by

$$t \gg \max \left(\frac{\ell_p^2}{\mathcal{D}_{O_2}}, \frac{1}{k_{1c} + k_{1a} + k_{2a} + k_{2c} \langle c_{O_2} \rangle^f} \right) \quad (\text{A.30})$$

it is not hard to deduce that both unsteady terms can be neglected in Eqs. (A.27a) and (A.27b) so that the closure problem becomes steady. Finally, since $\tilde{c}_{O_2} \ll \langle c_{O_2} \rangle^f$, it follows that $k_{2c} \tilde{c}_{O_2} \ll k_{1c} + k_{1a} + k_{2a} + k_{2c} \langle c_{O_2} \rangle^f$. As a consequence, Eq. (A.27a) yields $\tilde{c}_R \ll \langle c_{Re} \rangle_{sf}$ and the closure problem takes the form

$$\nabla^2 \tilde{c}_{O_2} = -\frac{\varepsilon_f^{-1} k_{2c} a_v}{\mathcal{D}_{O_2}} \langle c_{O_2} \rangle^f \langle c_{Re} \rangle_{sf} - \frac{\varepsilon_f^{-1} k_{2a} a_v}{\mathcal{D}_{O_2}} (\langle c_{Re} \rangle_{sf} - c_E^t) \quad \text{in } \mathbf{V}_f \quad (\text{A.31a})$$

$$-\mathbf{n} \cdot \mathcal{D}_{O_2} \nabla \tilde{c}_{O_2} = \mathbf{n} \cdot \mathcal{D}_{O_2} \nabla \langle c_{O_2} \rangle^f + k_{2c} \langle c_{O_2} \rangle^f \langle c_{Re} \rangle_{sf} + k_{2a} (\langle c_{Re} \rangle_{sf} - c_E^t) \quad \text{at } \mathbf{A}_{sf} \quad (\text{A.31b})$$

$$\tilde{c}_{O_2}(\mathbf{r}) = \tilde{c}_{O_2}(\mathbf{r} + \ell_{rev} \mathbf{e}_i) \quad (\text{A.31c})$$

This problem has a linear structure, so the solution on \tilde{c}_{O_2} can be sought in terms of a linear combination of the sources under the form

$$\tilde{c}_{O_2} = \mathbf{b} \cdot \nabla \langle c_{O_2} \rangle^f + s \langle c_{O_2} \rangle^f \langle c_{Re} \rangle_{sf} + h (\langle c_{Re} \rangle_{sf} - c_E^t) \quad (\text{A.32})$$

439 \mathbf{b} , s and h being the closure variables (note that \mathbf{b} is a vector whereas s and h are scalars)
440 which can be chosen to obey the following boundary value problems

Problem I

$$\nabla^2 \mathbf{b} = 0 \quad \text{in } \mathbf{V}_f \quad (\text{A.33a})$$

$$\mathbf{n} \cdot \nabla \mathbf{b} = -\mathbf{n} \quad \text{at } \mathbf{A}_{sf} \quad (\text{A.33b})$$

$$\langle \mathbf{b} \rangle^f = 0 \quad (\text{A.33c})$$

$$\mathbf{b}(\mathbf{r}) = \mathbf{b}(\mathbf{r} + \ell_{rev} \mathbf{e}_i) \quad (\text{A.33d})$$

441

Problem II

$$\nabla^2 s = -\frac{\varepsilon_f^{-1} k_{2c} a_v}{\mathcal{D}_{O_2}} \quad \text{in } \mathbf{V}_f \quad (\text{A.34a})$$

$$\mathbf{n} \cdot \nabla s = -\frac{k_{2c}}{\mathcal{D}_{O_2}} \quad \text{at } \mathbf{A}_{sf} \quad (\text{A.34b})$$

$$\langle s \rangle^f = 0 \quad (\text{A.34c})$$

$$s(\mathbf{r}) = s(\mathbf{r} + \ell_{rev} \mathbf{e}_i) \quad (\text{A.34d})$$

442

Problem III

$$\nabla^2 h = -\frac{\varepsilon_f^{-1} k_{2a} a_v}{\mathcal{D}_{O_2}} \quad \text{in } \mathbf{V}_f \quad (\text{A.35a})$$

$$\mathbf{n} \cdot \nabla h = -\frac{k_{2a}}{\mathcal{D}_{O_2}} \quad \text{at } \mathbf{A}_{sf} \quad (\text{A.35b})$$

$$\langle h \rangle^f = 0 \quad (\text{A.35c})$$

$$h(\mathbf{r}) = h(\mathbf{r} + \ell_{rev} \mathbf{e}_i) \quad (\text{A.35d})$$

443 Note that the conditions in Eqs. (A.33c), (A.34c) and (A.35c) result from the fact that
444 $\langle \tilde{c}_{O_2} \rangle^f = 0$ and are required for both closure problems to have a unique solution.

445 **Step 4: Macroscopic model**

446 When the representation of \tilde{c}_{O_2} is reported back into the average equation (A.24), one
447 finally obtains the following closed macroscopic equation for $\langle c_{O_2} \rangle^f$

$$\begin{aligned} \varepsilon_f \frac{\partial \langle c_{O_2} \rangle^f}{\partial t} &= \nabla \cdot (\varepsilon_f \mathbf{D}_{eff} \cdot \nabla \langle c_{O_2} \rangle^f) + \nabla \cdot (\mathbf{s} \langle c_{O_2} \rangle^f \langle c_{Re} \rangle_{sf}) \\ &+ \nabla \cdot (\mathbf{h} (\langle c_{Re} \rangle_{sf} - c_E^t)) \\ &- k_{2c} a_v \langle c_{O_2} \rangle^f \langle c_{Re} \rangle_{sf} - k_{2a} a_v \langle c_{Re} \rangle_{sf} + k_{2a} a_v c_E^t \end{aligned} \quad (\text{A.36})$$

with the effective parameters \mathbf{D}_{eff} and \mathbf{s} and \mathbf{h} given by

$$\mathbf{D}_{eff} = \mathcal{D}_{O_2} \left(\mathbf{I} + \frac{1}{V_f} \int_{\mathbf{A}_{sf}} \mathbf{n} \mathbf{b} dA \right) \quad (\text{A.37})$$

$$\mathbf{s} = \frac{\mathcal{D}_{O_2}}{V} \left(\int_{\mathbf{A}_{sf}} \mathbf{n} s dA \right) \quad (\text{A.38})$$

$$\mathbf{h} = \frac{\mathcal{D}_{O_2}}{V} \left(\int_{\mathbf{A}_{sf}} \mathbf{n} h dA \right) \quad (\text{A.39})$$

448 where \mathbf{b} , s and h are solution of the closure problems *I*, *II* and *III* in Eqs. (A.33), (A.34)
449 and (A.35) respectively. Note that in Eq. (A.37), \mathbf{D}_{eff} is a second order tensor and \mathbf{I} is the
450 identity ; $\mathbf{n} \mathbf{b}$ denotes the outer product between the two vectors \mathbf{n} and \mathbf{b} .

From Eq. (A.34b), the order of magnitude of s can be estimated to be $s = \mathbf{O}(k_{2c} \ell_p / \mathcal{D}_{O_2})$
and from Eq. (A.38), one gets $\mathbf{s} = \mathbf{O}(k_{2c})$. This leads to an order of magnitude estimate for
the second term on the right hand side of Eq. (A.36) given by $\nabla \cdot (\mathbf{s} \langle c_{O_2} \rangle^f \langle c_{Re} \rangle_{sf}) =$
 $\mathbf{O}\left(\frac{k_{2c}}{L} \langle c_{O_2} \rangle^f \langle c_{Re} \rangle_{sf}\right)$ while the order of magnitude of the macroscopic reactive term is
 $k_{2c} a_v \langle c_{O_2} \rangle^f \langle c_{Re} \rangle_{sf} = \mathbf{O}\left(\frac{k_{2c}}{\ell_p} \langle c_{O_2} \rangle^f \langle c_{Re} \rangle_{sf}\right)$ with the idea that $a_v = \mathbf{O}(\ell_p^{-1})$. The same
estimate can be made for \mathbf{h} . On the basis of the scale hierarchy, this indicates that the
macroscopic diffusion/reaction equation for $\langle c_{O_2} \rangle^f$ may finally be written as

$$\varepsilon_f \frac{\partial \langle c_{O_2} \rangle^f}{\partial t} = \nabla \cdot (\varepsilon_f \mathbf{D}_{eff} \cdot \nabla \langle c_{O_2} \rangle^f) - k_{2c} a_v \langle c_{O_2} \rangle^f \langle c_{Re} \rangle_{sf} - k_{2a} a_v \langle c_{Re} \rangle_{sf} + k_{2a} a_v c_E^t \quad (\text{A.40})$$

451 The average equation for $\langle c_{Re} \rangle_{sf}$ is given by Eq. (A.26).

452 **References**

- 453 [1] S. Reculusa, M. Heim, F. Gao, N. Mano, S. Ravaine, A. Kuhn, Design of catalytically
454 active cylindrical and macroporous gold microelectrodes, *Advanced Functional Materi-*
455 *als* 21 (4) (2011) 691–698.
- 456 [2] A. Karaji, S. Reculusa, M. Heim, P. Garrigue, S. Ravaine, N. Mano, A. Kuhn, Bottom-
457 up generation of miniaturized coaxial double electrodes with tunable porosity, *Advanced*
458 *Materials Interfaces* 2 (12) (2015) 1500192–1500196.
- 459 [3] A. Karajić, S. Reculusa, S. Ravaine, N. Mano, A. Kuhn, Miniaturized electrochemical
460 device from assembled cylindrical macroporous gold electrodes, *ChemElectroChem* 03
461 (2016) 2031–2035.
- 462 [4] T. Siepenkoetter, U. Salaj-Kosla, X. Xiao, P. Conghaile, M. Pita, R. Ludwig, E. Magner,
463 Immobilization of redox enzymes on nanoporous gold electrodes: Applications in biofuel
464 cells, *ChemPlusChem* 82 (4) (2017) 553–560.
- 465 [5] A. Walcarius, A. Kuhn, Ordered porous thin films in electrochemical analysis, *Trends*
466 *in Analytical Chemistry* 27 (2008) 593–603.
- 467 [6] R. Szamocki, S. Reculusa, S. Ravaine, P. N. Bartlett, A. Kuhn, R. Hempelmann,
468 Tailored mesostructuring and biofunctionalization of gold for increased electroactivity,
469 *Angewandte Chemie International Edition* 45 (8) (2006) 1317–1321.
- 470 [7] K. B. Blodgett, Films built by depositing successive monomolecular layers on a solid
471 surface, *Journal of the American Chemical Society* 57 (1935) 1007–1022.
- 472 [8] P. N. Bartlett, P. R. Birkina, M. A. Ghanema, Electrochemical deposition of macropo-
473 rous platinum, palladium and cobalt films using polystyrene latex sphere templates,
474 *Chemical Communications* 17 (2000) 1671–1672.
- 475 [9] S. Reculusa, S. Ravaine, Synthesis of colloidal crystals of controllable thickness through
476 the Langmuir-Blodgett technique, *Chemistry of Materials* 15 (2003) 598–605.
- 477 [10] D. Leech, P. Kavanagh, W. Schuhmann, Enzymatic fuel cells: Recent progress, *Elec-*
478 *trochimica Acta* 84 (2012) 223–234.
- 479 [11] A. de Poulpiquet, D. Ranava, K. Monsalve, M. T. Giudici-Ortoni, E. Lojou, Biohy-
480 drogen for a new generation of H_2/O_2 biofuel cells: A sustainable energy perspective,
481 *ChemElectroChem* 1 (2014) 1724–1750.
- 482 [12] M. Rasmussen, S. Abdellaoui, S. D. Minteer, Enzymatic biofuel cells: 30 years of critical
483 advancements, *Biosensors and Bioelectronics* 76 (2016) 91–102.
- 484 [13] S. Shleev, Quo vadis, implanted fuel cell?, *ChemPlusChem* 82 (2017) 522–539.

- 485 [14] N. Mano, A. de Poulpiquet, O_2 reduction in enzymatic biofuel cells, Chemical Reviews
486 118 (5) (2018) 2392–2468.
- 487 [15] E. Solomon, U. Sundaram, T. Machonkin, Multicopper oxidases and oxygenases, Chem-
488 ical Reviews 96 (1996) 2563–2605.
- 489 [16] X. Xiao, H.-Q. Xia, R. Wu, L. Bai, L. Yan, E. Magner, S. Cosnier, E. Lojou, Z. Zhu,
490 A. Liu, Tackling the challenges of enzymatic (bio)fuel cells, Chemical Reviews 119 (16)
491 (2019) 9509–9558.
- 492 [17] L. Wang, X. Wu, B.-W. Su, R. Song, J.-R. Zhang, J.-J. Zhu, Enzymatic biofuel cell:
493 Opportunities and intrinsic challenges in futuristic applications, Advanced Energy and
494 Sustainability Research (2021) 2100031.
- 495 [18] M. J. Moehlenbrock, S. D. Minteer, Extended lifetime biofuel cells, Chemical Society
496 Reviews 37 (2008) 1188–1196.
- 497 [19] S. D. Minteer, P. Atanassov, H. R. Luckarift, G. R. Johnson, New materials for biological
498 fuel cells, Materialstoday 15 (2012) 166–173.
- 499 [20] M. Cadet, S. Gounel, C. Stines-Chaumeil, X. Brilland, J. Rouhana, F. Louerat,
500 N. Mano, An enzymatic glucose/ O_2 biofuel cell operating in human blood, Biosensors
501 and Bioelectronics 83 (2016) 60–67.
- 502 [21] S. Cosnier, A. J. Gross, A. L. Goff, M. Holzinger, Recent advances on enzymatic glu-
503 cose/oxygen and hydrogen/oxygen biofuel cells: Achievements and limitations, Journal
504 of Power Sources 325 (2016) 252–263.
- 505 [22] M. Gamella, A. Koushanpour, E. Katz, Biofuel cells - activation of micro- and macro-
506 electronic devices, Bioelectrochemistry 119 (2018) 33–42.
- 507 [23] A. de Poulpiquet, A. Ciaccafava, E. Lojou, New trends in enzyme immobilization at
508 nanostructured interfaces for efficient electrocatalysis in bio fuel cells, Electrochimica
509 Acta 126 (2014) 104–114.
- 510 [24] C. E. Zhao, P. Gai, R. Song, Y. Chen, J. Zhang, J. J. Zhu, Nanostructured material-
511 based biofuel cells: recent advances and future prospects, Chemical Society Reviews
512 46 (5) (2017) 1545–1564.
- 513 [25] C. Stines-Chaumeil, E. Roussarie, N. Mano, The nature of the rate-limiting step of blue
514 multicopper oxidases: Homogeneous studies versus heterogeneous, Biochimie Open 4
515 (2017) 36–40.
- 516 [26] R. D. Levie, Electrochemical response of porous and rough electrodes, Advances in
517 Electrochemistry and Electrochemical Engineering 6 (1967) 329–397.

- 518 [27] O. E. Barcia, E. D'Elia, I. Frateur, O. R. Mattos, N. Pebere, B. Tribollet, Applica-
519 tion of the impedance model of de Levie for the characterization of porous electrodes,
520 *Electrochimica Acta* 47 (2002) 2109–2116.
- 521 [28] E. O. Barnes, X. Chen, P. Li, R. G. Compton, Voltammetry at porous electrodes: A
522 theoretical study, *Journal of Electroanalytical Chemistry* 720–721 (2014) 92–100.
- 523 [29] Z. Ban, E. Katelhon, R. G. Compton, Voltammetry of porous layers: Staircase vs analog
524 voltammetry, *Journal of Electroanalytical Chemistry* 776 (2016) 25–33.
- 525 [30] H. T. H. Chan, E. Katelhon, R. G. Compton, Voltammetry using multiple cycles: Porous
526 electrodes, *Journal of Electroanalytical Chemistry* 799 (2017) 126–133.
- 527 [31] P. D. Vidts, R. E. White, Governing equations for transport in porous electrodes, *Jour-
528 nal of the Electrochemical Society* 144 (1997) 1343–1352.
- 529 [32] T. R. Ferguson, M. Z. Bazant, Nonequilibrium thermodynamics of porous electrodes,
530 *Journal of The Electrochemical Society* 159 (2012) 1967–1985.
- 531 [33] M. Ender, An extended homogenized porous electrode model for lithium-ion cell elec-
532 trodes, *Journal of Power Sources* 282 (2015) 572–580.
- 533 [34] T. D. Le, D. Lasseux, X. P. Nguyen, G. L. Vignoles, N. Mano, A. Kuhn, Multi-scale
534 modeling of diffusion and electrochemical reactions in porous micro-electrodes, *Chemical
535 Engineering Science* 173 (2017) 153–167.
- 536 [35] T. D. Le, L. Zhang, G. L. Vignoles, N. Mano, A. Kuhn, D. Lasseux, Optimal thickness of
537 a porous micro-electrode operating a single redox reaction, *ChemElectroChem* 6 (2019)
538 173–180.
- 539 [36] T. Le, D. Lasseux, Current and optimal thickness predictions for a porous micro-
540 electrode, *ChemElectroChem* 7 (2020) 3017–3027.
- 541 [37] T. D. Le, L. Zhang, A. Kuhn, N. Mano, G. L. Vignoles, D. Lasseux, Upscaled model for
542 diffusion and serial reduction pathways in porous electrodes, *Journal of Electroanalytical
543 Chemistry* 855 (2019) 113325.
- 544 [38] S. Tsujimura, T. Nakagawa, K. Kano, T. Ikeda, Kinetic study of direct bioelectrocatal-
545 ysis of dioxygen reduction with bilirubin oxidase at carbon electrodes, *Electrochemistry*
546 72 (2004) 437–439.
- 547 [39] I. Mazurenko, K. Monsalve, J. Rouhana, P. Parent, C. Laffon, A. L. Goff, S. Szunerits,
548 R. Boukherroub, M. T. Giudici-Orticoni, N. Mano, E. Lojou, How the intricate interac-
549 tions between carbon nanotubes and two bilirubin oxidases control direct and mediated
550 O₂ reduction, *Applied Materials and Interfaces* 8 (2016) 23074–23085.

- 551 [40] J. Galceran, S. Taylor, P. Bartlett, Modelling the steady-state current at the inlaid
552 disc microelectrode for homogeneous mediated enzyme catalysed reactions, *Journal of*
553 *Electroanalytical Chemistry* 506 (2001) 65–81.
- 554 [41] P. Bartlett, K. Pratt, Theoretical treatment of diffusion and kinetics in amperomet-
555 ric immobilized enzyme electrodes part i: Redox mediator entrapped within the film,
556 *Journal of Electroanalytical Chemistry* 397 (1995) 61–78.
- 557 [42] T. Q. N. Do, M. Varničić, R. Hanke-Rauschenbach, T. Vidaković-Koch, K. Sundmacher,
558 Mathematical modeling of a porous enzymatic electrode with direct electron transfer
559 mechanism, *Electrochimica Acta* 137 (2014) 616–626.
- 560 [43] S. V. Hexter, F. Grey, T. Happe, V. Climent, F. A. Armstrong, Electrocatalytic mech-
561 anism of reversible hydrogen cycling by enzymes and distinctions between the major
562 classes of hydrogenases, *PNAS* 109 (2012) 11516–11521.
- 563 [44] S. V. Hexter, T. F. Esterle, F. A. Armstrong, A unified model for surface electrocatalysis
564 based on observations with enzymes, *Physical Chemistry Chemical Physics* 16 (2014)
565 11822–11833.
- 566 [45] S. Whitaker, *The method of volume averaging*, Kluwer Academic Publishers, Dordrecht,
567 The Netherlands, 1999.
- 568 [46] L. Rajendran, M. Kirthiga, E. Laborda, Mathematical modeling of nonlinear reaction-
569 diffusion processes in enzymatic biofuel cells, *Current Opinion in Electrochemistry* 1 (1)
570 (2017) 121 – 132.
- 571 [47] S. Brocato, C. Lau, P. Atanassov, Mechanistic study of direct electron transfer in bilirubin
572 oxidase, *Electrochimica Acta* 61 (2012) 44–49.
- 573 [48] J. A. V. Butler, The mechanism of overvoltage and its relation to the combination
574 of hydrogen atoms at metal electrodes, *Transactions of the Faraday Society* 28 (1932)
575 379–382.
- 576 [49] F. J. Valdés-Parada, D. Lasseux, S. Whitaker, Diffusion and heterogeneous reaction
577 in porous media: The macroscale model revisited, *International Journal of Chemical*
578 *Reactor Engineering* 15 (6) (oct 2017). doi:10.1515/ijcre-2017-0151.
- 579 [50] F. V. Parada, D. Lasseux, S. Whitaker, Upscaling reactive transport under hydrody-
580 namic slip conditions in homogeneous porous media, *Water Resources Research* 56 (1)
581 (2020) e2019WR025954. doi:10.1029/2019WR025954.
- 582 [51] D. Lasseux, F. J. Valdés-Parada, Symmetry properties of macroscopic transport co-
583 efficients in porous media, *Physics of Fluids* 29 (4) (2017) 043303. doi:10.1063/1.
584 4979907.

- 585 [52] F. Al-Lolage, P. Bartlett, S. Gounel, P. Staigre, N. Mano, Site-directed immobilization
586 of bilirubin oxidase for electrocatalytic oxygen reduction, *ACS Catalysis* 9 (3) (2019)
587 2068–2078.
- 588 [53] L. Zhang, C. Carucci, S. Reculosa, B. Goudeau, P. Lefrancois, S. Gounel, N. Mano,
589 A. Kuhn, Rational design of enzyme modified electrodes for optimized bioelectrocatalytic
590 activity, *ChemElectroChem* (2019) in press. doi:10.1002/ce1c.201901022.
- 591 [54] A. Baux, G. Couégnat, G. Vignoles, D. Lasseux, A. Kuhn, C. Carucci, N. Mano, T. Le,
592 Digitization and image-based structure-properties relationship evaluation of a porous
593 gold micro-electrode, *Materials and Design* 193 (2020) 108812. doi:10.1016/j.matdes.
594 2020.108812.
- 595 [55] R. Szamocki, A. Velichko, F. Mücklich, S. Reculosa, S. Ravaine, S. Neugebauer,
596 W. Schuhmann, R. Hempelmann, A. Kuhn, Improved enzyme immobilization for en-
597 hanced bioelectrocatalytic activity of porous electrodes, *Electrochemistry Communica-*
598 *tions* 9 (2007) 2121–2127.
- 599 [56] F. Valdés-Parada, C. Aguilar-Madera, J. Álvarez Ramírez, On diffusion, dispersion and
600 reaction in porous media, *Chemical Engineering Science* 66 (2011) 2177–2190.
- 601 [57] C. Truesdell, R. Toupin, *The classical field theories*, Springer-Verlag, New-York, 1960.
- 602 [58] W. G. Gray, A derivation of the equations for multi-phase transport, *Chemical Engi-*
603 *neering Science* 30 (1975) 229–233.

Declaration of interests

The authors declare that they have no known competing financial interests or personal relationships that could have appeared to influence the work reported in this paper.

The authors declare the following financial interests/personal relationships which may be considered as potential competing interests:

T. D. Le: Conceptualization, Model derivation, Software, Draft preparation, Writing, Reviewing, Editing. **D. Lasseux:** Conceptualization, Model derivation, Software, Draft preparation, Writing, Reviewing, Editing. **L. Zhang:** Samples preparation, Experiments, Draft preparation. **C. Carucci:** Samples preparation, Experiments, Draft preparation. **S. Gounel:** Samples preparation, Experiments. **S. Bichon:** Samples preparation, Experiments. **F. Lorenzutti:** Software, Draft preparation. **A. Kuhn:** Conceptualization, Experimental supervision, Draft preparation, Writing, Reviewing, Editing. **T. Šafarik:** Samples preparation, Experiments. **N. Mano:** Conceptualization, Experimental supervision, Draft preparation, Writing, Reviewing, Editing.

Journal Pre-proofs